PREDICTION OF AERODYNAMIC NOISE GENERATED BY

WIND TURBINE BLADES

By

Rohith Giridhar

Submitted to the graduate degree program in Aerospace Engineering and the Graduate Faculty of the University of Kansas School of Engineering in partial fulfillment of the requirements for the degree of Masters of Science.

Committee:

_____

Dr. Saeed Farokhi, Chairperson

_____

Dr. Ray Taghavi, Committee Member

_____

Dr. Shawn Keshmiri, Committee Member.

Date Defended: 05/09/2016

The Thesis Committee for Rohith Giridhar certifies that this is the approved version of the following thesis:

PREDICTION OF AERODYNAMIC NOISE GENERATED BY

WIND TURBINE BLADES

Committee:

_____

Dr. Saeed Farokhi, Chairperson

_____

Dr. Ray Taghavi, Committee Member

_____

Dr. Shawn Keshmiri, Committee Member.

Date Defended: 05/09/2016

Abstract

The preliminary step in the computational study of mitigating the aerodynamic noise generated by wind turbine blades involves accurate prediction of aerodynamic noise generated by a wind turbine rotor which can be used a basis for comparison. The NREL Phase VI HAWT rotor has been chosen to perform this study. This is achieved by first predicting the three dimensional flow field around the rotor through CFD analysis using SST k-ω turbulence model for wind speeds of 7m/s, 10m/s, 13m/s and 15m/s. CFD analysis has been performed using the rotating reference frame method at steady state conditions which resulted in predicting the flow field accurately with less computational time. The rotational periodic boundary condition with 180^0 symmetry has been used with which one blade has been simulated instead of two. This reduced the mesh size and thus computational costs to perform the CFD analysis. To validate the prediction of flow field obtained through CFD analysis, performance characteristics and aerodynamic characteristics such as torque generated and trends of pressure coefficients at different span locations are validated against the time averaged experimental results and other results pertaining to the same published in previous computational study.

The results obtained through CFD analysis show good agreement with both experimental results and previous computational results. Based on the trends of pressure coefficients predicted for different wind speeds we see that it is most accurate at a wind speed of 7m/s and this accuracy gradually decreases with increase in wind speed.

Once the flow field was accurately predicted, this was used to predict both the location and magnitude of aerodynamic noise generated by the blade using the Curle broadband noise source model. Aeroacoustic analysis indicates that major noise sources are located near the tip of the blade and it gradually decreases as we move towards its root. This trend is observed at all four wind speed conditions. It is also observed that with increase in wind speeds, there is increase in the intensity of noise generated by the blades and thus increase in Sound Power Level across the blade.

Acknowledgements

Firstly, I would like to thank my advisor, Dr. Saeed Farokhi for giving me the opportunity to work on this research project on applied aerodynamics under his guidance. I thank him for both his valuable advice and his constant support and encouragement that he gave me throughout this project. I would also like to thank him for all his invaluable guidance that I received throughout my Master's program.

I would like to thank the other member of my committee Dr. Ray Taghavi and Dr. Shawn Keshmiri for taking their time to review this thesis and for providing comments and suggestions.

I would like to thank Dr. Scott Schreck from the National Renewable Energy Laboratory for providing me with the experimental data necessary to validate this computational study.

I would like to thank Mrs. Kristin Renells, Mr. Robert Curry and Dr. Jennifer Delgado for giving me the opportunity to work for the Physics and Astronomy Department as a Graduate Teaching Assistant all these semesters which gave me a great experience and has also provided me with financial support during my Master's program.

Finally I would like to thank Mrs. Radha Giridhar, Mr. S. Giridhar, Sri. R. Seshadri and Ms. Amirtha Giridhar, my family. It was through their constant support, love and encouragement that I have been able to complete this Master's program.

Table of Contents

List of Figures

List of Tables

Nomenclature

Latin Letters

c	Local chord length of blade	m
c_0	Speed of sound	m/s
C_p	Coefficient of pressure	~
C_P	Coefficient of Power	~
C_T	Coefficient of Torque	~
f	Frequency of flow disturbance	Hz
I	Intensity of sound transmission	W/m^2
L	Blade span	m
L_p	Sound Pressure Level	dB
L_w	Sound Power Level	dB
$\dot{m}$	Mass flow rate	kg/s
n	Number of rotor blades	~
p	Local static pressure	Pa
p_∞	Ambient pressure	Pa
P	Power captured by the wind	W
r	Local radius of rotation of the blade	m
S	Planform area of blade	m^2
T	Torque generated by wind turbine	Nm
U	Local velocity on blade surface	m/s
V_∞	Wind speed	m/s

Greek Letters

λ	wavelength of flow disturbance	m
ρ	density	kg/m^3
ρ_∞	density of ambient air	kg/m^3
θ_p	blade pitch angle	deg
ω	angular velocity of blade rotation	rad/s

Abbreviations and Acronyms

BTU.....British Thermal Units

CAD ..... Computer Aided Drawing

CFD.....Computational Fluid Dynamics

FW-H .....Ffowcs Williams and Hawkings equation

GW.....Giga Watts

HAWT.....Horizontal Axis Wind Turibne

MW .....Mega Watts

NREL ..... National Renewable Energy Laboratory

RANS.....Reynolds Averaged Navier Stokes Equations

SAP ..... Acoustic Power per unit surface area

SST.....Shear Stress Transport

UAE ..... Unsteady Aerodynamics Experiment

3D..... Three dimensional

1. Introduction

The very first automatically operated wind turbine made for the purpose of generating electricity was invented by an Ohio based engineer, Charles Brush in the year 1888 [1]. This turbine had a 60 foot tower with a 56 foot rotor diameter and 144 blades made of cedar wood [2] to generate 12 kilowatts of power.

Fast forward about eighty years, the rise in oil prices and greater environmental awareness created a need to find suitable alternative electric power sources other than coal or natural gas and thus lead to a renewed interest in wind turbines and its research in the 1970s [3]. It was estimated by researchers that there is enough wind potential in the United States to replace 45 quads of primary energy annually to generate electricity [4]. One quad or 10^{15} BTUs is equivalent to the energy in 167,000,000 barrels of oil.

These lead to crating many wind farms in California in the early 1980s. The wind turbines used then had rudimentary controls, were unreliable and required extensive maintenance [5]. However, through the research programs of National Renewable Energy Laboratory and Sandia National Laboratories among others, there have been numerous developments in this field such as development of more efficient airfoils, understanding three dimensional aerodynamic phenomena using wind tunnel tests, understanding fatigue and structures and better blade manufacturing to mention a few [3].

In the year 2015 alone, the global wind power industry installed 63,013 MW led by China with 30,500 MW worth new installations of wind turbines. The US market reached 8.6 GW and Germany leading the European countries with 6 GW of new installations. [6]

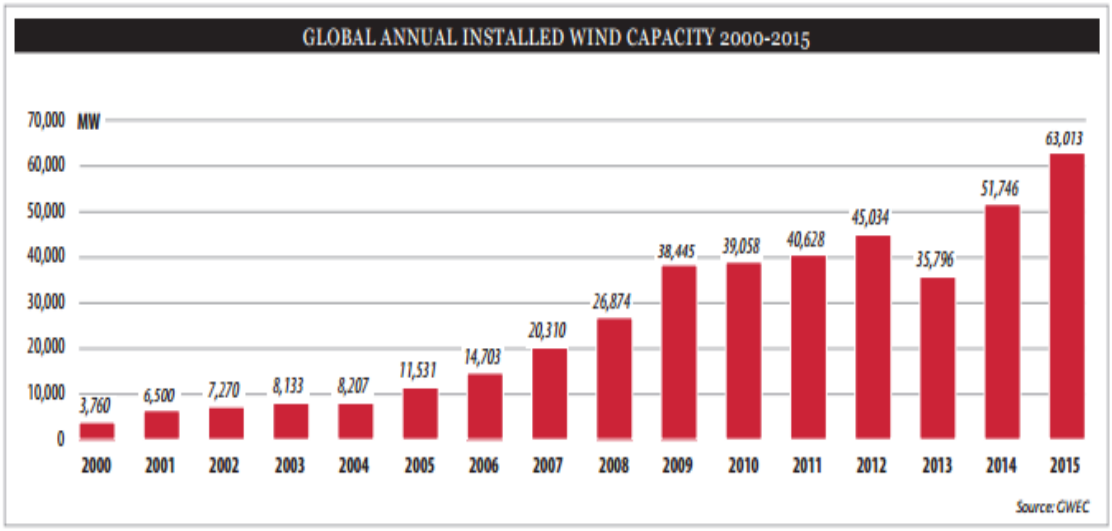

Figure 1: Global Annual Installed Wind capacity for 2000-2015, Global Wind Energy Council. [6]

Using wind energy as an alternative electric power source has led to reduction of millions of tons of carbon dioxide emissions annually.

The research and development in the field of wind turbine has been bolstered via Computational Fluid Dynamics and with growing computational capabilities in recent years. Studies such as blade performance analysis, aero-acoustic simulations and fluid-structure interactions can now be carried out on wind turbine blades which furthers our understanding in this field that involves complex three dimensional flow behaviors. This research is also one such study.

1.1 Classification of Wind Turbines

Wind turbines are broadly classified into two types namely:

a. Horizontal Axis Wind Turbines

Wind energy convertors which have their axis of rotation in a horizontal position and whose rotors are "propeller-like" are called Horizontal axis wind turbines [7]. In these turbines, the main rotor shaft and electrical generator is located on top of a tower. The rotor

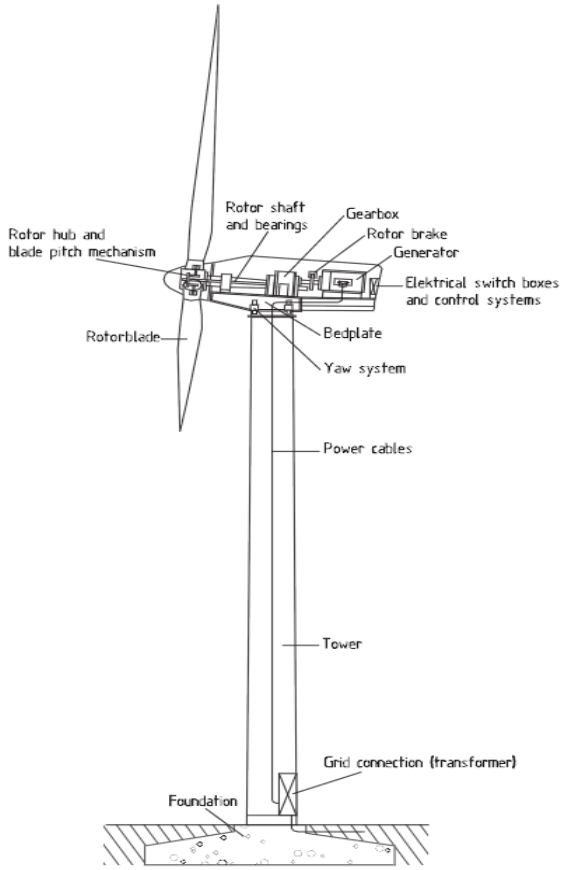

Figure 2: Schematic representation of a Horizontal Axis Wind Turbine. [7].

speed and power output of the turbine can be controlled by pitching rotor blades about their longitudinal axis. This also helps in protecting the wind turbines against over speeds and extreme wind speeds.

The shape of the blade is aerodynamically optimized by twisting the blade along its longitudinal axis which helps ensure a high efficiency of lift to drag ratio and thus achieve high torque. It is for these reasons that almost all wind turbines built for generating electricity are of horizontal axis type.

These turbines are classified into two configurations namely the downwind rotor and the upwind rotor. The terms denote the location of rotor with respect to the tower [8]. If the rotor is made to face the wind, this is referred to as upwind rotor configuration. If the rotor is made to face away from the wind and instead the nacelle and tower face the wind, such a configuration is referred to as the downwind rotor configuration.

b. Vertical Axis Wind Turbines

There are several types of vertical rotors with a vertical axis of rotation. In the beginning, the vertical axis rotors could be built only as a pure drag-type rotor. It has a symmetry configuration about the vertical axis which allows it to accept wind from any direction, so no yaw drive mechanism is needed.

The well-known examples of the vertical axis rotor is the “Savonius rotor” which can be found on railroad carriages and as cup anemometers to measure wind velocities.

Vertical axis rotors that work on the principal of lift was proposed by a French engineer Darrieus and the rotor has been named after him. This rotor in particular is considered a promising concept for modern wind turbines. In the “Darrieus rotor”, the blades are shaped and rotate in the pattern of a surface line on a geometric solid of revolution called *troposkien* (i.e. “turning rope” in Greek), with a vertical axis of rotation. This makes the geometric shape of the rotor blades complicated and thus difficult to manufacture. As is the case in horizontal axis rotors, Darrieus rotors are preferably built with two or three rotor blades [7, 8].

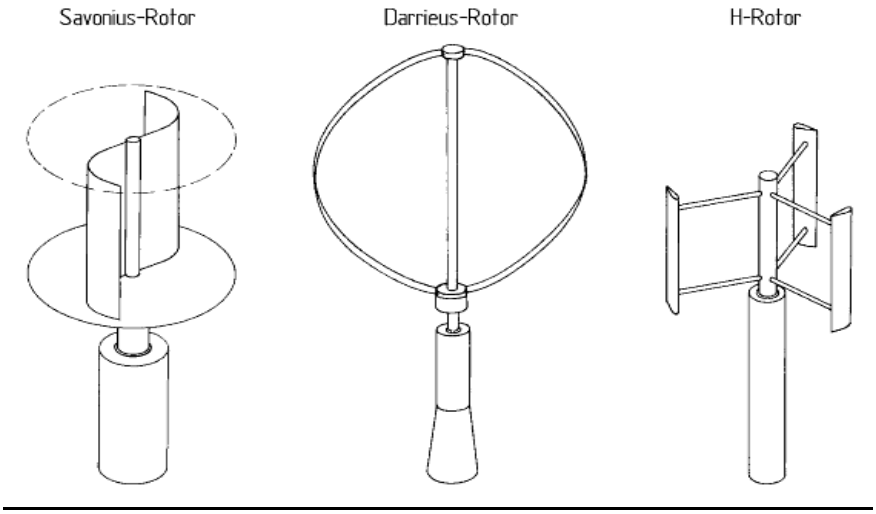

Figure 3: Schematic representations of Vertical Axis Wind Turbines [7]

1.2 Motivation and Objectives

With the use of wind turbine having benefits ranging from usage as an alternative source of electric power to positively impacting the environment by reducing greenhouse gas emissions, it becomes imperative for us to minimize its disadvantages. One such drawback associated with wind turbines is the noise it generates whose consequences are twofold namely, reduction in the efficiency of power extracted from incoming wind which is dissipated as aerodynamic noise and cause of annoyance and sleep disturbance to the people who live in its vicinity [9]. It has also been suggested that low frequency sound energy generated by wind turbines can directly impact health. So much so that many countries have regulations that stipulates wind turbines to be installed at distances significantly away from buildings or even go a step further and refuse to install wind turbines due to their negative impacts on humans [10].

Wind turbine noise is broadly classified into two namely mechanical noise and aerodynamic noise. Though mechanical noise has been reduced over a period of time through various vibration suppression and vibration isolation strategies, the aerodynamic noise arising from the trailing edge continues to be the most significant noise source. There have been techniques such as varying speed of rotation and increasing blade pitch angle which reduce the aerodynamic noise. However, this has been at the cost of significant power loss [11]

It is for these reasons that a computational study has been conducted to predict the aerodynamic noise generated by the different noise sources present on the blade. These results would later be used as a reference for comparison when performing the stage of computational analysis which involves mitigating the aerodynamic noise generated by wind turbines blade using elastomeric dampers without having significant detrimental impact on torque and thus power generated.

1.3 Overview of the thesis

The organization of this thesis is such that the literature review that includes existing experimental and computational studies on wind turbines is first introduced. Next an overview of concepts pertinent to wind turbine aerodynamics and wind turbine aero-acoustics is then introduced. The following section is the methodology which outlines steps involved in CFD and aeroacoustic analysis to predict aerodynamic noise generated. Finally the noise reduction study and computational technique to achieve the same is briefly introduced in Recommendations for Future work.

2. Literature Review

2.1 Literature review pertaining to CFD simulation of the NREL Phase VI rotor

There have been many CFD analysis that has been performed previously to predict the flow field for the NREL Phase VI rotor. Some of them have been included in this literature review and they have also been used for validation of this computational study.

2.1.1 Ece Sagol, Marcelo Reggio and Adrian Ilinca

Sagol et al [12] studied different two equations RANS turbulence models to predict flow characteristics and rotor performance using the NREL Phase VI rotor. The simulations were carried out under steady state flow conditions by implementing a rotating reference frame for fluid motion while keeping the blade stationary.

It was found that among the different RANS turbulence models, the SST k-ω model predicts the trends of pressure coefficients at different sections of the blade most accurately when compared to experimental results. This accuracy decreased with increasing wind speeds.

The low speed shaft torque is under predicted by 20% over the wind speed range though its trend has remained the same as that of the experiment. This is attributed to the CFD tool's poor capability to predict drag when flow separates or at low speeds, where drag is the main contributor to LSST. The root flap bending moment, on the other hand, has been predicted with high accuracy.

2.1.2 Jang Oh MO, Young-Ho Lee

J. O. MO et al [13] predicted the aerodynamic characteristics and blade performance of the NREL Phase VI wind turbine using the SST k-ω model. An initial height of 0.2mm was chosen in the normal direction away from the blade surface in the normal direction to ensure an average y+ value of 7 at 7m/s along the blade span. A hexahedral mesh was created.

The results indicated that the trend of pressure coefficients showed good agreement at 7m/s even though there is weak flow separation at the blade root.

The pressure coefficients also showed reasonably good agreement at 15m/s and 25m/s at different span locations of the blade indicating how robust the choice of SST k-ω model is.

The blade torque shows good agreement with the experimental results with errors ranging from 0.08% to 24.7%. The flow separation gradually increases from root to tip of the blade with increasing wind speeds ensuring the torque remains around the same magnitude from 10m/s onwards and thus is stall regulated.

2.1.3 N.N Sorensen, J.A Michelsen, S. Schreck

Sorensen et al [14] simulated the NREL Phase VI rotor using two different meshes. The first one is a free configuration consisting of a large domain and the second one being a cylindrical tunnel configuration.

A structured mesh using blocks were created such that the y+ value on the blade surface was less than 2 throughout.

For the free configuration, both steady and unsteady state simulations were carried out and there was little difference observed in the two results. Even though the time dependent behavior may be caused by large time step size used, limitations due to computing time

prevents further time step refinement. It was thus decided to opt out of unsteady state simulations.

The tunnel configuration mesh predicted results with the same accuracy as the free configuration.

There is a good qualitative agreement with the measurements on the prediction of the pressure coefficients except at 10m/s where the flow behavior is believed to be unstable.

The root flap bending moment shows good agreement with experimental results, whereas the low speed shaft torque is over predicted by 20% and at deep stall, the low speed shaft torque is under-predicted by 20%.

2.1.4 Y. Song and J.B Perot

CFD simulations of the NREL Phase VI rotor for a wind turbine configuration of 3^0 tip pitch, 0^0 yaw and 72 rpm was simulated using the Spallart Allmaras model [15].

An unstructured mesh with about 10 million cells were created. The y+ value is chosen such that it falls within the laminar sub viscous layer. A rotating cylindrical mesh placed in a domain of the same dimensions as the wind tunnel was created.

The trends of pressure coefficient at wind speeds below 10m/s are accurate and this accuracy drops beyond 10m/s.

The trend of low speed shaft torque is qualitatively accurate. However there is a discrepancy in their magnitude. Stream lines indicate significant flow separation at 10m/s and 21m/s.

2.1.5 R P J O M van Rooij and E A Arens

The NREL Phase VI blade was simulated using ANSYS-Fluent for a 0^0 yaw and 3^0 pitch rotor configuration [16]. A structured mesh with 4 blocks has been created such that the first height normal to the blade surface is $4*10^{-2}$mm to ensure a y+ value of about 1 throughout the blade surface.

The hemispherical domain with radius equal to 6 blade lengths was created containing a single blade and 180^0 symmetry configuration is used. The simulation was carried out using SST k-ω model for both steady and unsteady conditions and using DES model for unsteady conditions. There was little difference in results observed in all these three cases.

For speeds below 10m/s when the flow is attached, the pressure distributions predicted at different span locations on the blade are very close to experimental results. This accuracy decreases with increase in wind speeds due to flow separation. These results generally tend to be poor near the root but keep improving as we move close to the tip of the blade.

2.2 Literature review pertaining to wind turbine noise

Literature review in this section covers experimental studies to predict aerodynamic noise produced by wind turbine blades and both experimental and computational studies to predict aerodynamic noise perceived by a given observer in the far field region. Though previous work on aeroacoustic simulations have focused on predicting far field noise, prediction of aerodynamic noise sources on the blade surface, which is pertinent to our final goal of mitigating aerodynamic noise generated by the blade, was not available. It is for this reason that the current computational study has been conducted, and the results presented in this study can be used as a reference for comparison during our study of aerodynamic noise mitigation on the wind turbine rotor.

2.2.1 Masoud Ghasemian and Amir Nejat

Ghasemian et al[17] predicted the far field aerodynamic noise of the NREL Phase VI blade. The aero-acoustic simulation was conducted using Ffowcs Willams and Hawking's analogy. To perform this, the unsteady results from the Improved delayed detached eddy simulations and SST k-ω model was used.

To achieve this, the time dependent surface pressure fluctuations were used as the acoustic source field data. These are converted to frequency domain using Fast Fourier Transforms (FFT).

Simulations were performed for 7, 10 and 15m/s. The Improved Delayed Detached Eddy simulation model predicts trends of pressure coefficients at different span locations of the blade better than SST k-ω model and thus is more suitable for highly separated flows.

The prediction from SST k-ω model differs from experimental especially at 30% span of blade at 15m/s and at 46.6% span of blade at 10m/s when flow separation is significant in this region. Thickness and loading noise are found to be dominant noise sources.

Noise amplitude was found to increase with increasing wind velocity and decreasing distance of receiver from source.

2.2.2 A. Tadamasa and M. Zangeneh

Tadamasa et al[18] performed aero-acoustic simulations of the NREL Phase VI blade. The CFD results obtained using SST k-ω model and these results were used to obtain noise sources that were used in the F-W H analogy to predict the noise at a given observer's location.

According to the IEC 614000-11 international standard the observer was located along the axis of the wind turbine at a distance of (D/2 +H) along the base of the wind turbine tower.

where,

D-diameter of wind turbine rotor.

H-Height of tower.

The trends of pressure coefficients were accurate at low speeds. But with increasing speeds, the inaccuracy of model to predict flow separation lead to discrepancy in the trends of pressure coefficient especially on the suction side of the blade near its leading edge.

The aero-acoustic simulations for the case of 72 rpm corresponding to a tip Mach number of 0.12 indicates that quadrupole noise sources are not important noise sources.

At 72 rpm, loading noise is the dominant noise source and it increases with increasing wind speeds.

2.2.3 Seunghoon Lee and Soogab Lee

Seunghoon Lee et al [19] performed both numerical and experimental analysis to predict aerodynamic noise produced by small wind turbine blades. This analysis shows that trailing edge bluntness noise is an important aerodynamic noise source.

2.2.4 R.C Ramachandran, G. Raman and R.P Dougherty

Ramachandran et al [20] measured the noise generated from a 1.5MW wind turbine blade using compact microphone array. It was possible to identify those ranges of the frequency spectrum where one of aerodynamic noise or mechanical noise was dominant. The major component of noise is present in the lower end of the frequency spectrum ranging from 200Hz to 5000Hz and the sound pressure level keeps increasing with increasing frequency.

From 500Hz to 900Hz the dominant noise source is aerodynamic noise. Between 1000Hz to 1500Hz, it is observed that the dominant source is the mechanical noise from nacelle and weak aerodynamic noise from blade. At frequencies higher than 1500Hz, the aerodynamic noise grows closer in amplitude to mechanical noise. At around 5000Hz, the aerodynamic noise is about the same amplitude as mechanical noise.

From about 9000Hz, the aerodynamic noise reduces to a very low amplitude and above 10,000Hz no useful noise data can be estimated.

2.3 Literature review pertaining to experimental work on NREL Phase VI rotor

NREL performed experiments on the Phase VI rotor for many wind turbine configurations using the wind tunnel at NASA Ames Research Center in May 2000. The cross-section area of the wind tunnel (24.4m*36.6m) wind tunnel is so large that the blockage effects caused by the wind tunnel is negligible [21].

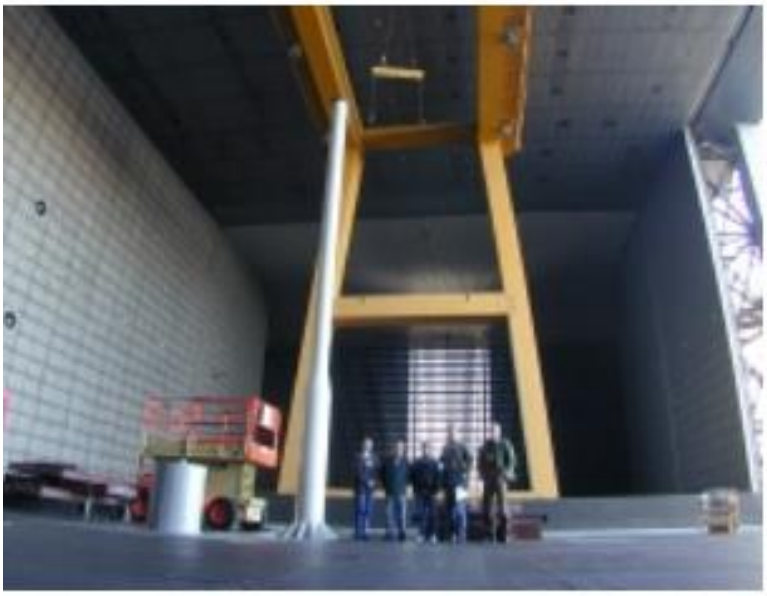

Figure 4: Wind Turbine tower present in the 24.4*36.6m NASA Ames wind tunnel [21]

NREL revealed all of their experimental results and information regarding the shape of the blade which can be used to verify the accuracy of many of the commercial codes available to predict wind turbine aerodynamic-characteristics. It is for this sake that the NREL Phase VI blade has been chosen for our analysis.

Figure 5: NREL Phase VI rotor [21]

The CAD model has been created using STARCCM+ and the blade specification required to create the geometry of the blade has been represented graphically below.

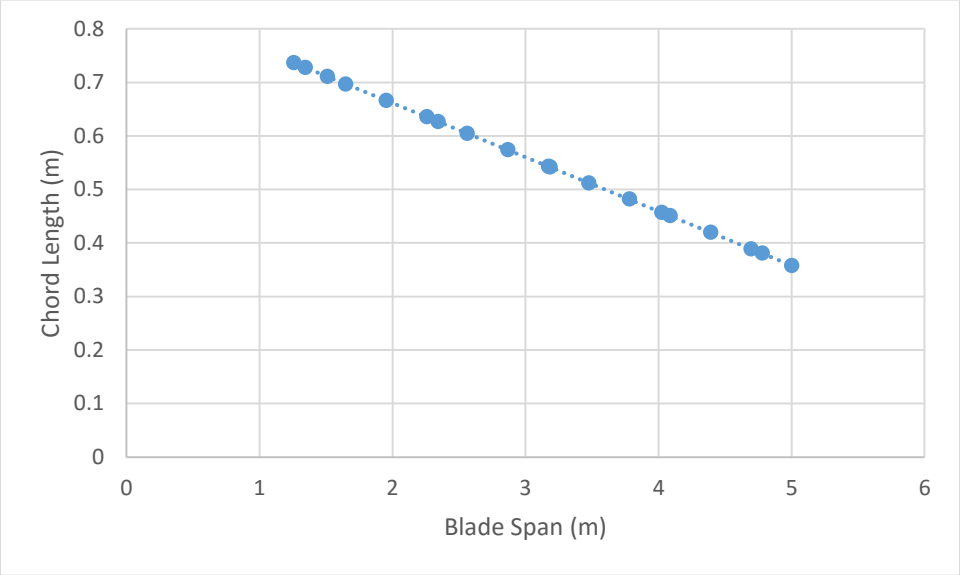

Figure 6: Linear chord length variation along the blade span.

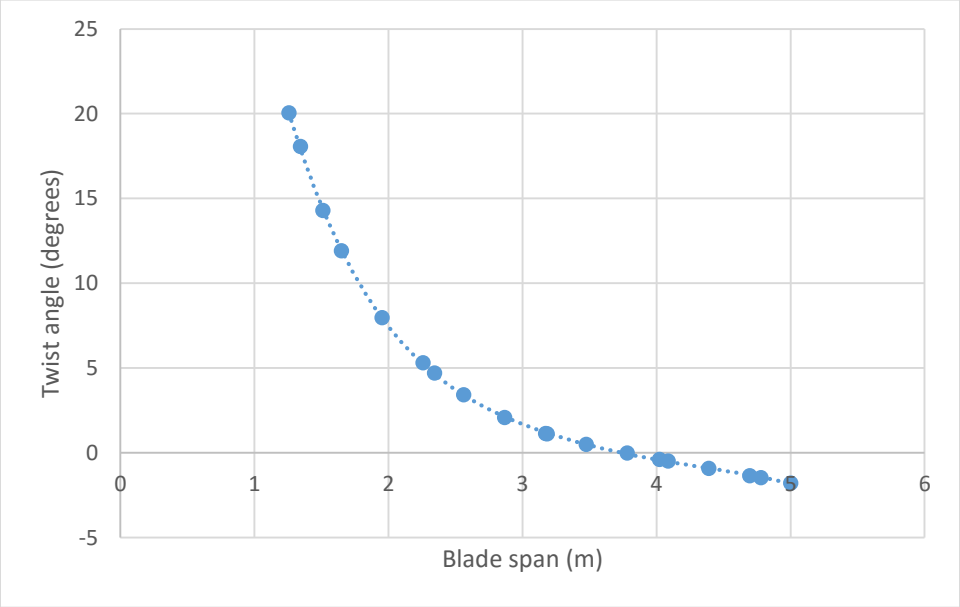

Figure 7: Non-Linear twist angle variation along the blade span

Number of blades	2
Rotor Diameter	10.048m
Airfoil	S809
Rotor speed	72 rpm counter clockwise direction
Pitch angle	3^0 towards feather
Yaw angle	0^0
Pitch axis	0.3c
Airfoil thickness	0.21c

Table 1: Specifications of the blade required to create the CAD model

The rotor blade used for our simulation is 5.029m long without its tip attachment. This blade transitions from a circular shaft section to an airfoil section from 0.883m to 1.2573m.

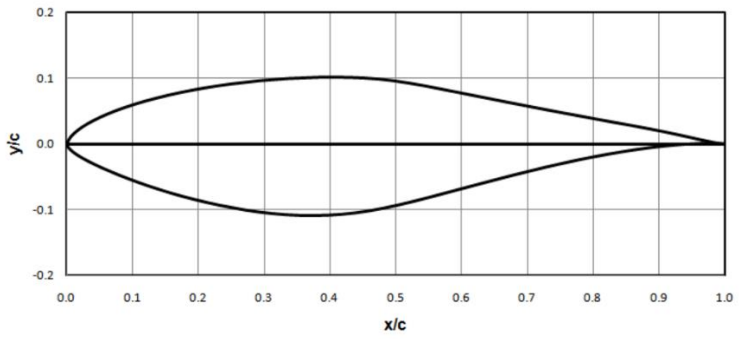

Figure 8: S809 Airfoil coordinates [22]

All relevant operating conditions at the six different wind speeds necessary to perform the simulations were kindly provided by Dr. Scott Schreck and their time averaged values have been tabulated below. During these simulations, the turbulent viscosity ratio used was 0.5 as indicated in [23].

Wind speed (m/s)	Density (kg/m^3)	Viscosity (kg/ms)	Ambient pressure (Pa)
7	1.2262	$1.796*10^{-5}$	101132.0
10	1.2293	$1.792*10^{-5}$	101131.1
13	1.2331	$1.788*10^{-5}$	101132.7
15	1.2320	$1.796*10^{-5}$	101114.4

Table 2: Operating conditions used at different wind speeds

3. Wind Turbine Aerodynamics

This section treats the operation of Horizontal Axis Wind Turbine (HAWT) machines only since we have used the same for our analysis. The conversion of wind energy to electric power is obtained through several mechanical systems. According to the air screw theory, the lift force is considered as the main driving force which produces the necessary torque. The shaft transfers the torque from the blades to the generator which is then output as electric energy [24].

Based on their mechanical configurations wind turbine set ups can be classified into three [25]:

a. Danish concept of a classical turbine with gearbox:

   It consists of a gearbox and with typically three steps it connects the slow rotating rotor shaft to the fast rotating generator shaft. This is in turn connected to the electrical grid and thus has a fixed rotational speed. These turbines are usually stall regulated rather than using active aerodynamic controls.

b. Turbine without gearbox, with the axle directly connected to the generator:

   A more novel concept of turbine set up where the turbine can be incorporated with a large multi-pole generator which allows the shaft to rotate with the low speed rotor.

c. A hybrid concept that combines the previous two.

   This concept is achieved by using a small generator and a small (generally 1 step) gearbox to obtain the desired angular speed.

Wind turbine may also be classified into

1. Fixed Speed Machines.
2. Variable Speed Machines.

Fixed Speed Machines

The wind turbines operate at a fixed angular velocity and it is not possible to regulate their speed with changing operating conditions or changing wind speeds. This is so because the machines lack the variable transmission mechanism required for rotor speed regulation.

Variable Speed Machines

Variable speed wind turbines, on the other hand, have the ability to operate at different rotor speeds so that maximum power can be extracted from the incident wind. As expected, these turbines are more expensive than the fixed speed machines as they have additional components to achieve rotor speed regulation.

These wind turbines operate over a range of wind speeds. The turbines begin to operate at what is referred to as cut in speeds which is about 3-5m/s. As wind speed increases, the power extracted by the wind turbine also increases until it reaches the rated power of the wind turbine which refers to the maximum power it is capable of capturing from the incident wind. Beyond this wind speed, the power extracted would be regulated until wind speeds reach about 25m/s referred to as cut off speeds where the turbine is brought to a halt using suitable braking mechanisms. For wind speeds beyond 25m/s, the wind is kept in "parked position" where the blades are made to remain stationary to avoid blade damage due to high thrust loads exerted on them. To ensure optimum power is extracted from the incident wind, different control mechanisms are used namely:

1. Pitch regulation.
2. Stall regulation.

Pitch Regulation

Pitch regulated wind turbines have an active control system where the blades can be pitched about its axis using electrical motors. This in turn changes the angular speed with which the blade rotates which alters the torque produced and thus power extracted. If the wind speed is greater than the cut off speed, then the blade is made to pitch such that it produces lesser lift and more drag due to increased flow separation. By doing so, the power extracted at higher wind speeds can be maintained at the rated power of the wind turbine.

Pitch regulated turbines see an increasing power trend from the cut in speed until it reaches the rated power of the wind turbine. Beyond this wind speeds, the power extracted in maintained at a constant value until the cut off wind speeds are attained. At this point, the pitch regulation mechanism is no longer able to control the rotor angular speed at which point the rotors of the turbine are brought to a halt [26]. The power curve of a pitch regulated wind turbine is represented by the solid line shown in Figure 4.

Stall Regulation

Stall regulated wind turbines operate such that when the wind speeds are high, with increase in wind speeds, the rotor angular velocity would decrease. This is so because the blades have been designed such that significant amount of flow separation takes place at these wind speeds. The blade initially begins to stall near its hub which gradually propagates along the span of the blade towards the tip. This in turn results in lesser torque generated by the blade and thus lesser power extracted from the wind at high wind speeds.

Since this method does not require any active control mechanisms to regulate the power extracted from the incident wind, it is more cost effective when compared to pitch regulated

wind turbines. The dotted line in Figure 4 represents the power curve of a stall regulated wind turbine.

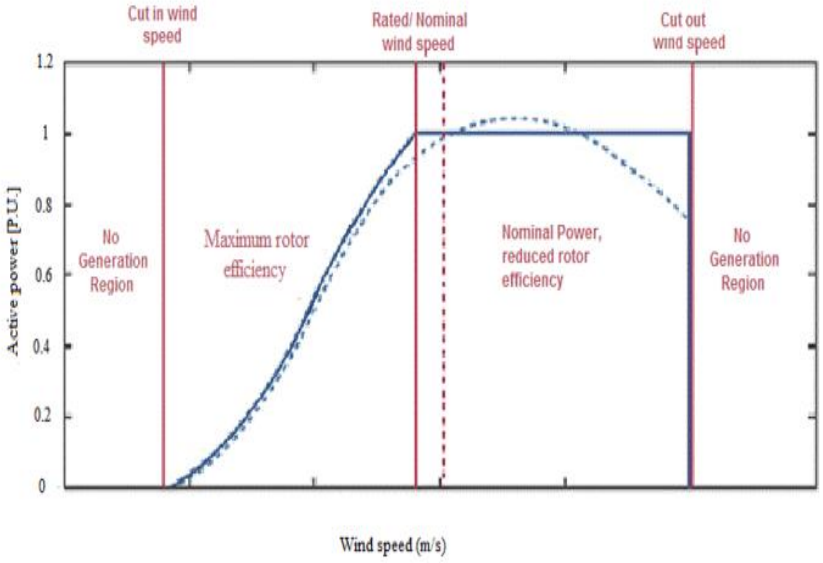

Figure 9: Power curve for Pitch regulated and Stall regulated Wind Turbines [27]

3.1 Aerodynamic Models

The size of commercial wind turbines has significantly increased in the past thirty years. We have come a long way from wind turbines with a rated power of 75kW with 17m rotor diameter to today's wind turbines whose rotor diameters are as enormous as 125m that have a rater power of 5MW. It has been predicted that the turbine size would continue to increase up to 250m in the future. The scaling up of the turbine to reduce costs has been effective so far. However, it is not clear if this trend will continue [28]. With higher power ratings, the focus of the wind industry is shifting towards offshore development of these turbines [24].

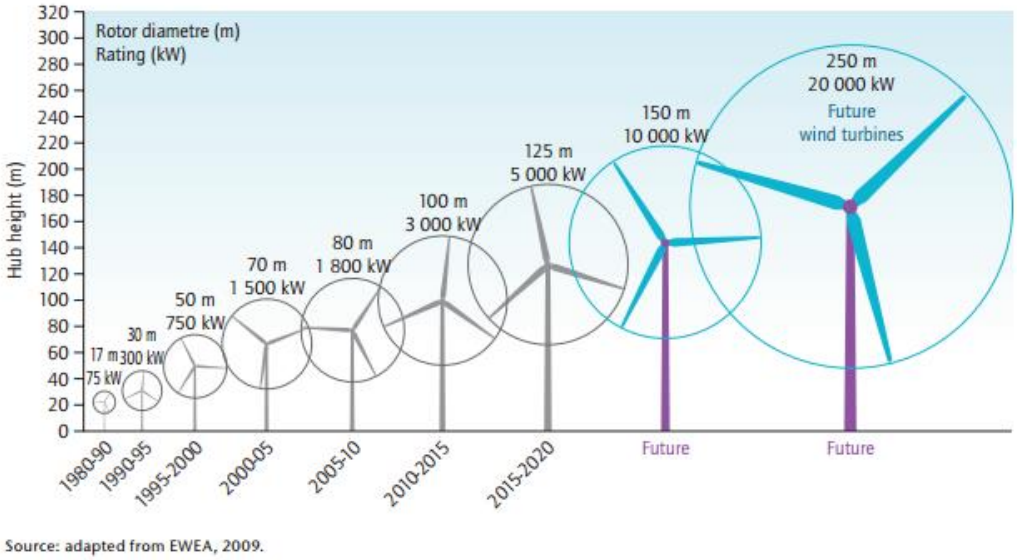

Figure 10: Growth in size of wind turbine over the years [28]

There are number of aerodynamic models that have been used to analyze wind turbines. Some of these models are listed below:

i. Blade Element Momentum Theory (BEM)

ii. Lifting line, panel and vortex methods

iii. Actuator disc theory

iv. Navier Stokes solvers (in CFD based approach)

We shall focus on the methodologies used by Navier Stokes solvers as this has been employed for the current research. Before this, some basic definitions that have been used during methodology shall be introduced.

3.2 Basic Definitions

i. Pressure Coefficient

Pressure coefficient is a non-dimensional number that relates the local static pressure relative to ambient pressure with the corresponding dynamic pressure. In general, while representing plots of pressure coefficient against different locations of an airfoil section, it is plotted as a negative value.

The pressure coefficient is thus defined as

$$C_p = \frac{(p - p_\infty)}{\frac{1}{2}\rho_\infty((r\Omega)^2 + (V_\infty)^2)^{0.5}} \tag{3.1}$$

ii. Power Coefficient

Consider a stream tube of air moving with free stream velocity V_∞. If the cross section area of this stream tube is A and the mass of air flowing in this stream tube be m then its kinetic energy is given by

$$E = \frac{1}{2}mV_\infty^2 \tag{3.2}$$

and for a unit mass,

$$e = \frac{1}{2}V_\infty^2 \tag{3.3}$$

If V is the volume of the stream tube and its volume flow rate is Q, then

$$Q = V_\infty A \tag{3.4}$$

and the mass flow rate for air with density ρ_∞ is

$$\dot{m} = \rho_\infty Q = \rho_\infty V_\infty A \tag{3.5}$$

The product of kinetic energy per units mass and mass flow rate is the available power contained in the wind. i.e.

$$P_o = \dot{m}e = \frac{1}{2}\rho_\infty V_\infty^3 A \tag{3.6}$$

If P is the power captured by the wind turbine rotor from this wind, then the power coefficient is defined as

$$C_P = \frac{P}{\frac{1}{2}\rho_\infty V_\infty^3 A} \tag{3.7}$$

According to Betz, the power coefficient cannot exceed a maximum value of 16/27 [25].

iii. Torque coefficient

If the integral torque acting on the rotor of planform area S and blade span L is T, then its torque coefficient is defined as

$$C_T = \frac{T}{\frac{1}{2}\rho_\infty V_\infty^2 SL} \tag{3.8}$$

3.3 CFD Techniques

Computational Fluid Dynamics is the branch of fluid mechanics where numerical analysis is employed to problems that involve fluid flows [29]. It is based on conservation laws governing fluid flow namely conservation of mass, momentum and energy [30].

CFD has been used to analyze wing and rotor configurations as early as the 1980's with unsteady Euler solvers introduced during these times. Full-RANS equations were then used to solve for helicopter rotor configurations taking viscous effects into account and the first full Navier-Stokes computations of rotor aerodynamics were performed during the late nineties. More recently, the Detached Eddy Simulation and Large Eddy Simulation techniques have been used for computational studies. Though these techniques offer high accuracy in flow prediction, they have a downside of high computational requirement [25].

For the work under taken in this thesis, Computational Fluid Dynamics has been utilized to validate performance characteristics and aerodynamic characteristics of a small scale wind turbine (NREL Phase VI rotor) for the case when there was no elastomeric damper used on the blade to mitigate aerodynamic noise. These were namely torque, bending moment and trends of pressure coefficients at different blade span locations. Once these parameters were validated against the experimental data and other CFD simulations for the same rotor obtained from literature, the broad band noise was then predicted using Aero-acoustic simulations

CFD is based on conservation laws namely the conservation of mass, conservation of momentum and conservation of energy which have been mentioned below using tensor notations respectively.

$$\frac{\partial \rho}{\partial t} + \frac{\partial \left(\rho u_j\right)}{\partial x_j} = 0 \tag{3.9}$$

$$\frac{\partial(\rho u_j)}{\partial t} + \frac{\partial}{\partial x_j}\left(\rho u_i u_j + \partial_{ij} p - \tau_{ij}\right) = 0 \tag{3.10}$$

$$\frac{\partial(\rho E)}{\partial t} + \frac{\partial}{\partial x_j}(\rho H u_j + q_j - \tau_{ij}) = 0 \tag{3.11}$$

In the above equations, ρ represents static density, p represents static pressure, u_i represents the velocity, E represents the total enthalpy per unit volume, H represents the total enthalpy per unit volume (i.e. sum of total internal energy and pressure-volume work, τ_{ij} is the stress tensor and q_{ij} is the heat flux vector.

Flow nature can be either laminar or turbulent based on the Reynolds number at which it operates. A laminar flow can be described using the continuity and momentum equations whereas the turbulent flow is characterized by fluctuations in fluid and thus associated with different length scales. These governing equations contain a nonlinear convection term and a non-local pressure gradient term [24].

To solve these equations, there are many turbulence models being used among which the Reynolds Averaged Navier Stokes Equations are commonly used in literature due to their robust abilities to predict CFD results at the expense of reasonable computational costs. Some of the commonly used RANS models are Spalart-Allmaras model, k-ε 2-equation model, k-ω 2-equation model, Menter's k-ω SST model and 7 equation RANS turbulence model to mention a few.

For this computational study, the k-ω SST turbulence model has been chosen for our analysis, the choice for which will be justified in the literature review section.

3.3.1 k-ω SST turbulence model

Among the different eddy viscosity turbulence models, it is known that the k-ω turbulence model is a robust and accurate model in predicting the flow field in the near-wall regions. Whereas, the k-ε turbulence model has displayed free-stream independence in the far field region. Menter developed a turbulence model which incorporates the advantages of both these models into a single model. To achieve this, the k-ε model is converted into the k-ω formulation. This turbulence model is referred to as the Shear Stress Transport k-ω Turbulence model [30]. The SST k-ω model is similar to the standard k-ω model, but it includes certain refinements. One of the main refinements is that the standard k-ω model and the transformed k-ε model are both multiplied by a blending function and both these models are added together. The blending function has a value of 1 in the near-wall region and this in turn activates the standard k-ω model. When the blending function has a value of 0 away from the surface, the k-ε model is then activated [31].

SST k-ω model has found to be more accurate for a wide class of flow regimes such as adverse pressure gradient flows, airfoils, transonic shock waves when compared to the standard k-ω model.

The SST k-ω model also incorporates the definition of turbulence viscosity so that it can account for the turbulent shear stress. The SST k-ω model equations are given as follows [24]:

$$\frac{\partial(\rho k)}{\partial t} + \frac{\partial(\rho k u_i)}{\partial x_j} = \frac{\partial}{\partial x_j}\left(\Gamma_k \left(\frac{\partial k}{\partial x_j}\right)\right) + G_k - Y_k + S_k \tag{3.12}$$

$$\frac{\partial(\rho \omega)}{\partial t} + \frac{\partial(\rho \omega u_i)}{\partial x_i} = \frac{\partial}{\partial x_j}\left(\Gamma_\omega \left(\frac{\partial \omega}{\partial x_j}\right)\right) + G_\omega - Y_\omega + S_\omega + D_\omega \tag{3.13}$$

where,

G_k represents the generation of turbulence kinetic energy due to mean velocity gradients.

G_ω represents the generation of ω

Y_k, Y_ω represents the disspation of k and ω

S_k, S_ω represents user defined source terms

Γ_k, Γ_ω represents the diffusivity of k and ω

D_ω represents the cross diffusion term

4. Wind Turbine Noise

We characterize sound by rapid small scale pressure fluctuations overlying the normal atmospheric pressure. These fluctuations propagate through a medium in the form of sound waves [20]. In fluids, sound propagates as longitudinal waves and thus the medium becomes periodically denser and rarer. This corresponds to higher and lower pressures respectively. These pressures are perceived by an observer located at a certain distance from the source and is referred to as "sound pressure" which is a function of time. If this sound is perceived as unwanted and unnecessary, it is referred to as noise.

Noise emitted by Wind turbines are broadly classified into

- Mechanical Noise
- Aerodynamic Noise

4.1 Mechanical Noise

Mechanical noise originates from the relative motion of mechanical components of a wind turbine and dynamic response among them. This noise is transmitted along the structure of the turbine and radiated from different surfaces such as the nacelle or casing.

Some of the components that are major contributors to mechanical noise are gearbox, generator and cooling fans. The hub and rotor would transmit the noise from these sources through noise radiation. [32]

Based on their transmission path, mechanical noise is classified into two

a. Air-borne noise

This noise is directly propagated from the component that produces the noise into the air.

b. Structure-borne noise

The structure-borne noise is first transmitted along the surface of different structural components which is in the proximity of the noise source. This noise is then radiated from another surface of the wind turbine.

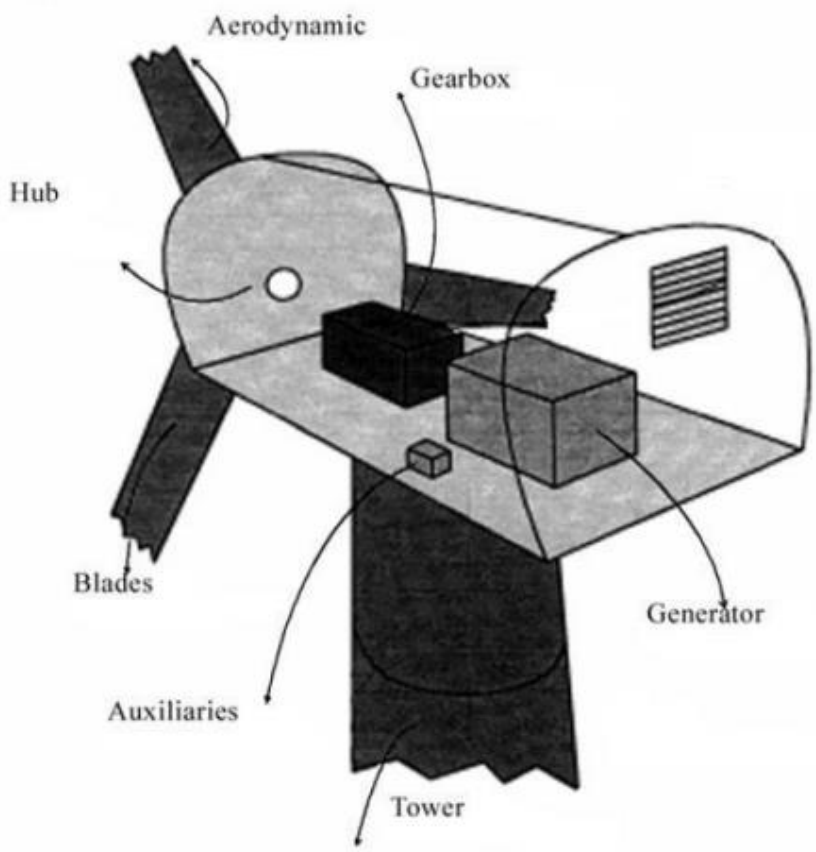

Figure 11: Various noise sources from a wind turbine [32, modified]

Many different steps have been taken to reduce mechanical noise. Some of them are nacelle insulation, vibration isolation of different machinery parts and the enveloping nacelle, damping of transmission paths and replacing spur gears by quieter helical gears. Through these steps, it has been possible to reduce mechanical noise to an extent that the aerodynamic noise is now the major noise source.

Since this research work is focused on aerodynamic noise prediction with the intention of mitigating the same, this topic would be discussed in more detail in the next section.[32]

4.2 Aerodynamic Noise

Aerodynamic noise is radiated from the blades and mainly associated with the interaction between turbulence and the blade surface. This turbulence may already be present in the incoming flow due to atmospheric turbulence or may arise due to viscous flow in the boundary layer formed around the blades. Turbulence may also arise when the incident flow on the wind turbine comes from the downstream of a preceding rotor.

Initially the boundary layer forming on the blade may be laminar. However, for high chord based Reynolds number of around 1-5 million, transition from laminar to turbulent flow is expected.

The flow initially is accelerated near the leading edge of the blade as it moves along the airfoil section until it reaches the point corresponding to critical pressure coefficient where the local Mach number is the highest. Beyond this point, the flow decelerates. This, in addition to adverse pressure gradient causes the flow to separate from the surface.

Furthermore, the boundary layers on the pressure side and the suction side of the blade merge together beyond the trailing edge to form the wake, which is associated with vortex shedding from the blade.

Finally, since the blade span is finite, the pressure difference present between the suction side and pressure side tend to compensate at the blade tip. This results in the flow to cross over the side edge of the tip which results in the formation of tip vortices.

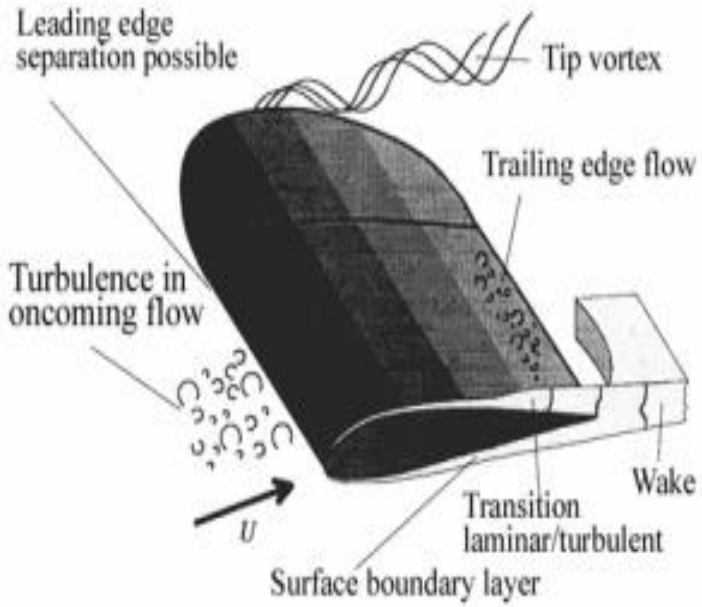

Figure 12: Flow around the rotor blade [32].

These different flow behaviors induce aerodynamic noise through different mechanisms which have been broadly classified into three types and are explained below. [32]

4.2.1 Low frequency Noise

When the wind turbine operates, it encounters certain changes in the flow due to the presence of the tower. This effect is seen both upstream and downstream of the flow. The upstream flow gets decelerated, whereas in case of the downstream flow, the flow is unable to remain attached to the tower contour and experiences separation. This in turn results in wake formation and thus velocity deficit in the vicinity of the tower.

As the blades rotate about their axis, they encounter the flow field generated by the tower. At this point, there is a rapid change in the blade loading due to which noise occurs.

This noise generated is a discrete frequency noise and is a function of blade passing frequency and number of blades. This type of noise is significant only when the Mach number is significantly high (~0.5).

This noise generated due to blade-tower interaction contributes only to the low frequency noise. [20]

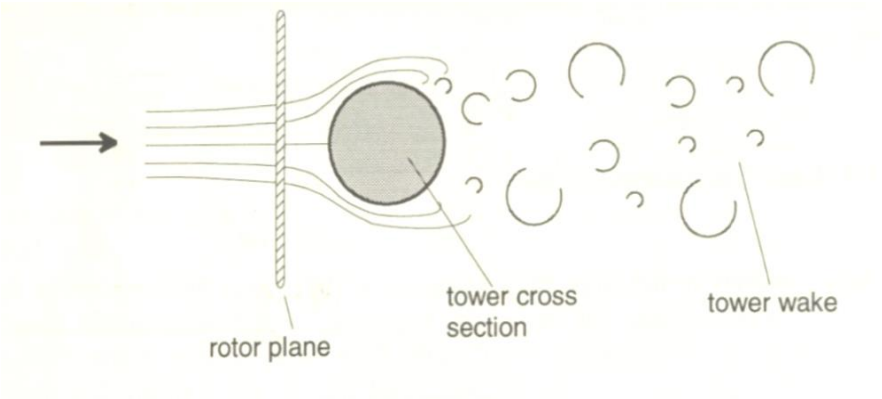

Figure 13: Flow around a cylindrical wind turbine tower for upwind configuration [32]

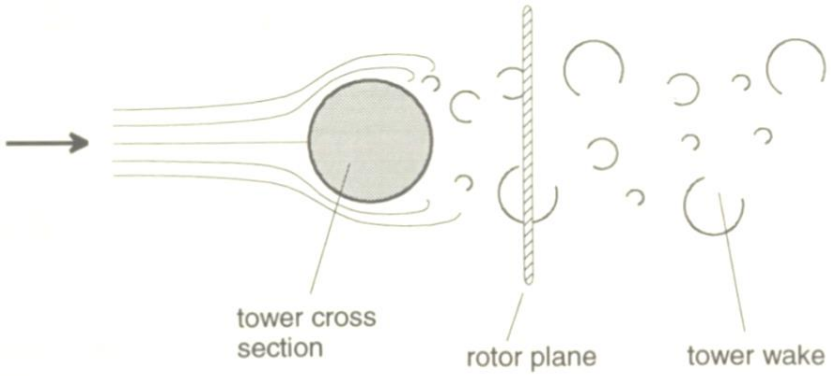

Figure 14: Flow around a cylindrical wind turbine tower for downwind configuration [32]

4.2.2 Inflow-Turbulence Noise

The incoming flow that is incident on the blade may already be turbulent in nature. This turbulence occurs in the flow due to the viscous nature of air and thus leads to formation of atmospheric boundary layer. In the boundary layer exchange of momentum takes place due to viscous and turbulent shear stresses. This results in the formation of turbulent eddies.

Turbulence occurs because of two reasons namely aerodynamic turbulence and thermal turbulence. Aerodynamic turbulence occurs when flow interacts with the surface, in this case the ground and thermal turbulence occurs when air is heated locally by the sun which leads to buoyancy.

If the local velocity at the blade is represented by U and the size of the eddy is represented by λ, then the frequency of disturbance is given by

$$f = \frac{U}{\lambda} \tag{4.1}$$

Based on this frequency, inflow turbulence noise can be further classified into

i. Low-frequency inflow-turbulence noise

If the size of eddy is much larger than the blade chord, then this will affect the global aerodynamic force acting on the blade. This will cause a noise radiation which is proportional to the sixth power of the local Mach number. Since the size of these eddies are large, the frequency associated with them are low and the wavelength associated with this noise disturbance is much larger than the blade chord.

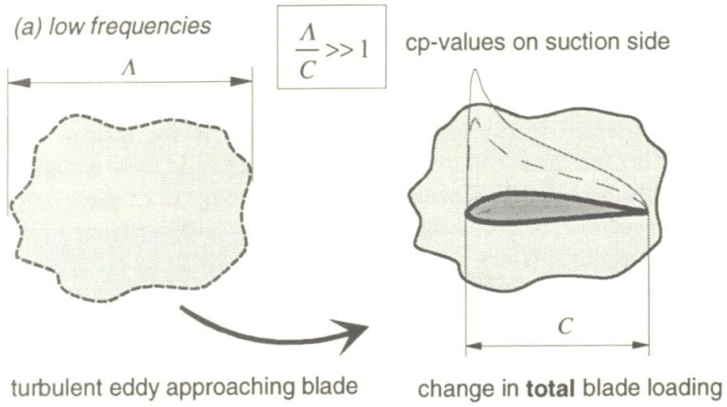

Figure 15: Low frequency in flow turbulence noise [32]

ii. High-frequency inflow-turbulence noise

If the size of the eddy is comparable or much smaller than the blade chord, this will result in only a local pressure fluctuation and will not affect the global aerodynamic load. Furthermore, the frequency of radiated noise is proportional to fifth power of local Mach number [32].

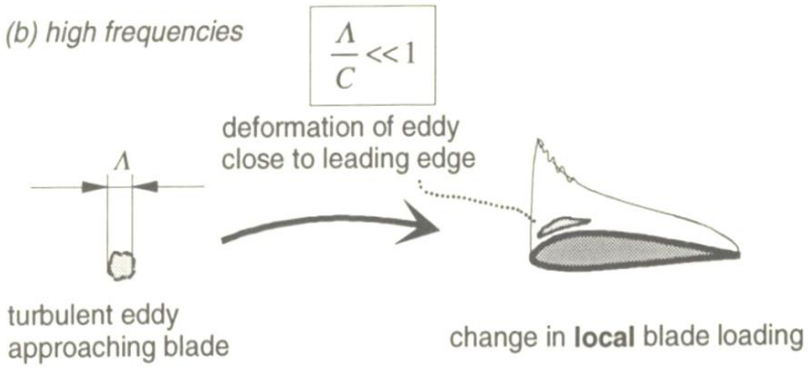

Figure 16: High frequency inflow turbulence noise [32]

4.2.3 Airfoil Self Noise

Due to instabilities present within the boundary layer and due to interaction of eddies present in the boundary layer with the airfoil surface, Airfoil self-noise occurs.

Based on different mechanisms, airfoil self-noise can be classified into:

a. Trailing edge noise

The boundary layer begins to form starting from the stagnation point near the leading edge of the blade. This boundary layer will gradually transition from laminar to turbulent. This takes place at certain chord wise location on the blade whose position depends upon several factors such as airfoil profile shape, angle of attack, operating Reynolds number, structure of the surface, the length scale of the turbulence eddies, the kinetic energy possessed by these eddies and eddy convection velocities.

At low Mach numbers, these turbulent eddies are inefficient sound sources. However, when these turbulent eddies come close to a sharp edge, in this case the trailing edge of the blade, the interaction of these eddies with the trailing edge of the blade make them a significant noise source.

The trailing edge noise has been found to be the dominant noise source especially in the high frequency region of the aerodynamic noise spectrum.

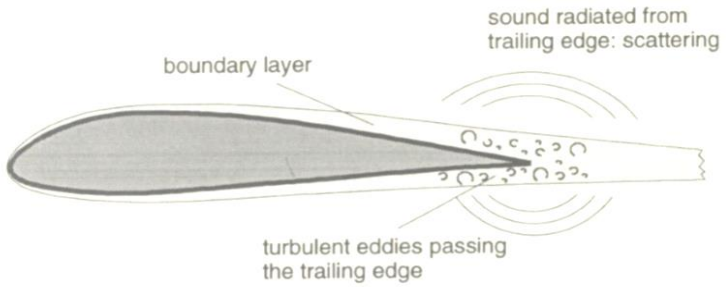

Figure 17: Trailing edge noise [32]

b. Laminar Boundary Layer Vortex Shedding Noise

If a wind turbine rotor blade operates such that its Reynolds number varies from 100,000 to 1 million, then the laminar boundary layer may extend upto the trailing edge of the blade. There are many instabilities present in the laminar to turbulent transition region of the blade. These instabilities are referred to as the "Tollmien-Schlichting instabilities" which interact with the acoustic wave field coming from trailing edge and results in a tonal noise.

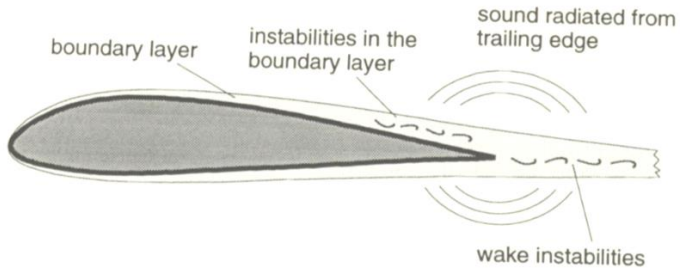

Figure 18: Laminar boundary layer vortex shedding noise [32]

b. Tip Noise

At the tip of the blade, the pressure differences present between the suction surface and the pressure surface result in cross flow to occur at the side edge of the tip. This results in the formation of tip vortex. These tip vortices interact with the trailing edge of the blade and thus cause tip noise.

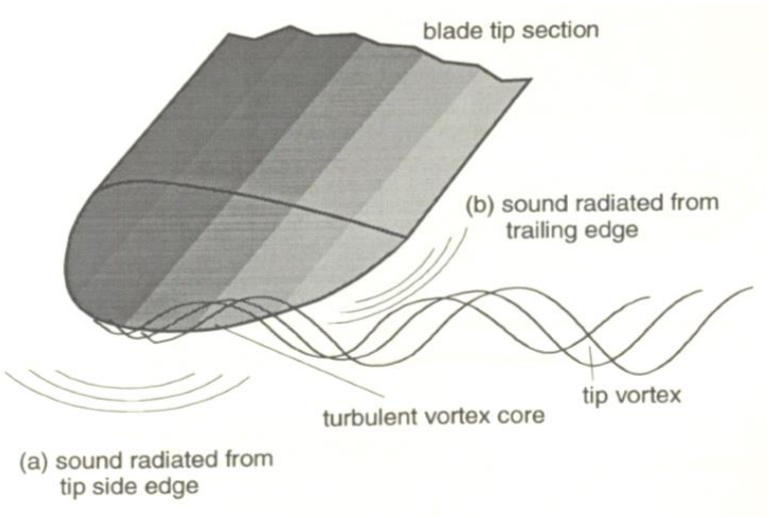

Figure 19: Tip noise [32]

c. Stalled Flow Noise

With increase in angle of attack, there is higher unsteadiness in the flow, beyond which point the flow separates and the blade experiences stall. Depending upon the extent of blade stall, the noise characteristics would also change. In other words, noise characteristics would vary from a single trailing edge radiation in case of small scale stall to a full chord radiation in case of deep stall.

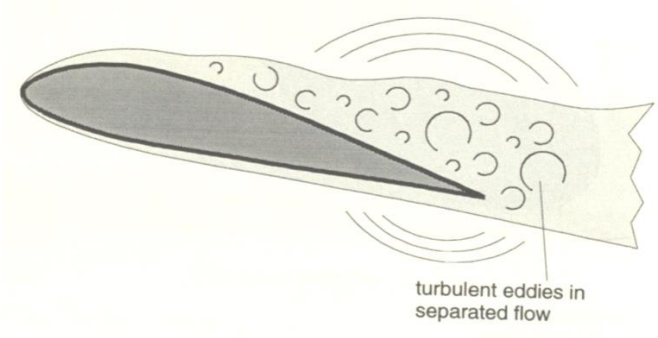

Figure 20: Stalled flow noise [32]

d. Blunt Trailing edge noise

A blunt trailing edge may also cause vortex shedding which in turn results in noise radiation which is of tonal nature. This type of noise can be reduced by ensuring that the trailing edge is sufficiently sharp.

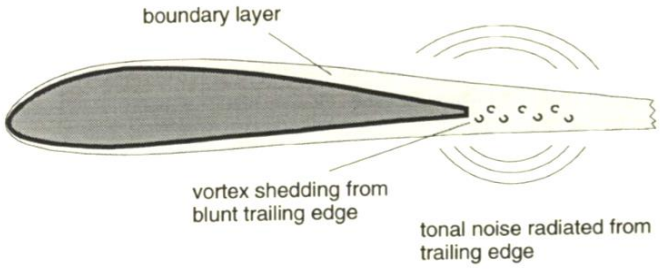

Figure 21: Blunt trailing edge noise [32]

4.3 Basic Definitions

a. Sound Pressure Level

The human ear is does not respond linearly to amplitude of sound pressure, i.e. doubling the amplitude of sound pressure does increase its loudness but does not make it sound doubly loud but far less than that. It is for this reason that it is customary to represent sound pressure level in a logarithmic scale. The sound pressure level is thus defined as

$$L_p = 10 \log_{10}\left(\frac{\hat{p}^2}{\hat{p}_{ref}^2}\right) \tag{4.2}$$

In the above equation, p is the root mean square sound pressure which is defined by

$$\hat{p}^2 = \lim_{T\to\infty}\left(\frac{1}{T}\right)\int_0^T (p^2(t)dt) \tag{4.3}$$

And $\hat{p}_{ref} = 2.10^{-5}\ Pa$ a standard reference pressure corresponding to weakest audible sound.

Sound pressure level is a property of sound at a given observer's location and can be measured by a single microphone.

b. Sound Power Level

The total strength of a sound source can be characterized by the sound power that is emitted from this source. If 'S' represents the surface which encloses the sound source through which the sound is transmitted with an intensity 'I', then sound power is given by

$$P = \int_S IdS \tag{4.4}$$

The definition of sound power level is thus given by

$$L_w = 10.\log_{10}\left(\frac{P}{P_{ref}}\right) \tag{4.5}$$

where the reference sound power is $P_{ref} = 10^{-12}\ W$.

Sound power level is a property of source of sound as it gives the total acoustic power emitted by the source.[32]

c. Tonal Noise

Tonal noise, also referred to as discrete frequency noise consists of spectral tones that are pure tones in nature. Pure tones are wave forms that occur only at a single frequency. Tonal noise is typically associated with a rotating object with known rotational speed at a predictable frequency [33].

d. Broadband Noise

Broadband noise has a frequency spectrum where there is no discrete tones that are present. The sound pressure fluctuations of broad band noise are not periodic and have random phases and amplitudes associated with it [33].

e. Monopole source

A monopole sound source radiates sound equally well in all directions [34]. The sound field it generates is radially symmetric and depends only on its distance from the source.

f. Dipole source

A dipole source consists of two monopole source of equal strength but have an opposite phase and are separated by a small distance. This distance is comparable to the wavelength of the acoustic wave. Since the two sources are out of phase, while one source expands, the other source contracts. It is for this reason that the dipole does not radiate noise equally in all directions [34].

g. Quadrupole source

Two opposite dipoles make up a quadrupole source. Quadrupoles come in two types namely the Lateral Quadrupole arrangement where the two dipoles do not lie along the same line and Linear Quadrupole arrangement where the two dipoles lie along the same line [34].

4.4 Linear Wave Equation

The generation and propagation of aerodynamic sound is governed by the three conservation laws namely the conservation of mass, conservation of energy and conservation of momentum.

For an inviscid fluid, the conservation of mass and momentum (the Euler equation) can be represented respectively as

$$\frac{\partial \rho}{\partial t} + \frac{\partial (\rho u_j)}{\partial x_j} = 0 \tag{4.6}$$

And

$$\frac{\partial (\rho u_j)}{\partial t} + \frac{\partial}{\partial x_j}(\rho u_i u_j) + \frac{\partial p}{\partial x_i} = 0 \tag{4.7}$$

By partially differentiating the above two equations with respect to time and combining the two equations we get

$$\frac{\partial^2 \rho}{\partial t^2} - \frac{\partial^2}{\partial x_i \partial x_j}(\rho u_i u_j) - \frac{\partial^2 p}{\partial x_i^2} = 0 \tag{4.8}$$

In the above equation, the acoustic quantities p, ρ and u_i can be written in terms of uniform quantities when fluid is at rest such as uniform pressure p_0, uniform density ρ_0, and uniform velocity in the ith direction 0 along with their corresponding perturbations i.e. p', ρ' and u_i' respectively. Substituting these in equation (3.8) we get

$$\frac{\partial^2 (\rho_0 + p')}{\partial t^2} - \frac{\partial^2}{\partial x_i \partial x_j}\left((\rho_0 + \rho')u_i' u_j'\right) - \frac{\partial^2 (p_0 + p')}{\partial x_i^2} = 0 \tag{4.9}$$

This equation in turn reduces to

$$\frac{\partial^2 \rho'}{\partial t^2} - \frac{\partial^2 p'}{\partial x_i^2} = 0 \tag{4.10}$$

By assuming that the pressure fluctuations that occur in the fluid due to compression and expansion is isentropic, acoustic pressure can be related to acoustic density as

$$p' = c_0^2 \rho' \tag{4.11}$$

where is the velocity with which the disturbance propagates through the medium.

Thus the homogenous wave equation in terms of acoustic pressure obtained using equations (3.10) and (3.11) are

$$\left(\frac{1}{c_0^2}\right)\left(\frac{(\partial^2 p')}{\partial t^2}\right) - \frac{\partial^2 p'}{\partial x_i^2} = 0 \tag{4.12}$$

The inhomogeneous form of the above wave equation can be written as

$$\left(\frac{1}{c_0^2}\right)\left(\frac{(\partial^2 p')}{\partial t^2}\right) - \frac{\partial^2 p'}{\partial x_i^2} = \sigma \tag{4.13}$$

where σ represents an arbitrary source term.

The above equation has been represented in the time domain. It may also be represented in terms of frequency domain using Fourier Integrals.

4.5 Aeroacoustics

Aeroacoustics is the branch of acoustics that investigates the aerodynamic generation of sound [35]. A theory was derived by Sir James Lighthill to predict the intensity of sound that is radiated from turbulent flow. According to this theory, the actual flow field that is responsible for generating noise is replaced by equivalent system of noise sources that are governed by standard acoustic propagation equations. This theory was referred to as the aeroacoustic analogy.

This theory was further developed by Curle, who later extended the concepts proposed by Lighthill's such that it could include the effect of flow body interaction on sound propagation.

Curle's acoustic model focused on predicting the aerodynamic noise sources and location of the same on given body accurately.

Later on Lighthill's theory was further extended by Ffowcs-Williams and Hawkings to predict the far field noise accurately which is useful in the field of helicopter and turbine industries.

Nowadays there are numerous models that are used for performing aeroacoustic analysis.

Aeroacoustic models can be broadly classified into three categories namely:

a. Broadband Noise Source Models

Broadband noise source models are used to compute the location and strength of the main noise sources. These noise sources are categorized into two namely the volume distribution of quadrupole noise sources and surface distribution of dipole noise sources. To compute the location and strength of the noise sources, the flow field quantities obtained from the Reynolds Averaged Navier Stokes Equations are used. It is for the same reason the computational time for using Broadband noise source model is small. To predict the dipole

generated noise per unit surface, the Curle's broadband noise source model is used. To predict the quadrupole generated noise per unit volume, the Proudman's broadband noise source model is used.

b. Far field noise predicting models for rotating bodies

Ffowcs Williams and Hawkings is a method used in aeroacoustic analysis that is used to predict far field noise using near field flow data that has been obtained through unsteady CFD analysis. The method uses integral formulations obtained using Green's functions to predict the far field noise as opposed to predicting the noise using direct noise simulation.

A special case of this method can be implemented on rotating bodies where steady state CFD results can be used to predict the far field noise. By the use of rotating reference frame, an unsteady CFD case is converted into a steady CFD case by treating the rotating body as stationary relative to the incoming flow.

Brentner and Farassat [36] modified the original Ffowcs Williams and Hawkings equation such that can use the steady state flow field quantities obtained through CFD analysis to predict far field noise for rotating bodies. In this case, the incident flow must be parallel to the axis of rotation of the body.

c. Noise predicting models using unsteady CFD results

Since in most cases which involve noise prediction, noise would be an unsteady phenomenon, a transient CFD analysis is required in such cases to predict aero acoustic noise. Typically a CFD analysis is performed by treating the flow as a compressible flow after which direct noise simulation is employed to predict aerodynamic noise accurately. The drawback of this simulation is that a very fine mesh is needed to perform aero acoustic analysis.

Another approach that uses flow field prediction that was obtained through unsteady CFD analysis is the Ffowcs Williams and Hawkings equation. This model uses the concept of Lighthill's acoustic analogy for predicting far field noise.

Ffowcs Williams and Hawkings model is further classified into two namely the Permeable FW-H model where the quadrupole noise sources are included while predicting the total noise and the Impermeable FW-H model where the quadrupole noise source is neglected due to their insignificant contribution to total noise at especially in flow regimes which involve low Mach numbers.

Among the different acoustic models available, the Curle broadband noise source model has been chosen to perform aeroacoustic analysis and predict the aerodynamic noise generated by the wind turbine rotor. Prediction of far field noise is not necessary for this study because our final goal is to mitigate the aerodynamic noise generated by the blade and the results obtained through this broadband noise source model will be our basis for comparison. Since literature review indicates that quadrupole noise sources are only significant when Mach numbers in the flow regime are greater than 0.5 [18] as in the case of helicopter blades, we did not focus on predicting the quadrupole sources using the Proudman's broadband noise source model.

4.5.1 Curle Broadband Noise Source Model

The Curle broadband noise source model is used to predict the noise generated when the flow present in the turbulent boundary layer interacts with a solid body (a dipole noise source) at low Mach numbers. The model computes the surface acoustic power to determine the local distribution of the total acoustic power per unit area of the body surface area [38].

This model has been used to predict broad band noise sources in various applications such as air handling sub systems, rotating parts such as blowers, heat exchangers, mufflers, distribution ducts to mention a few.

This model can be used for both steady and unsteady CFD simulations and is compatible with all RANS models that provides turbulence time and length scales. This model can also be used along with coupled flow solver and segregated flow solver.

The model uses the Curl integral which is based on Lighthill's acoustic analogy and is given by

$$p'(\vec{x},t) = \left(\frac{1}{4\pi a_0}\right)\int_S \left[\left(\frac{\vec{x}-\vec{y}}{r^2}\right)\left(\frac{\partial p}{\partial t}\right)\left(\bar{y}\,, t-\left(\frac{r}{a_0}\right)\right)\right]\vec{n}dS(\vec{y}) \tag{4.14}$$

And the local contribution of acoustic power per unit surface area is given by

$$SAP = \int_S (\, I(\vec{y})dS(\vec{y}) \tag{4.15}$$

where,

$t-\left(\frac{r}{a_0}\right)$ is the emission time

A_c is the correlation area

p is the surface pressure

p’ is the acoustic pressure

a_0 is the far field sound speed

$r = \vec{x} - \vec{y}$

I(y) is the directional acoustic intensity per unit surface

Finally the acoustic power per unit surface is given by

$$SAP\ (dB) = 10\log(\ SAP/P_{ref}\ ) \tag{4.16}$$

where p_{ref} is the reference acoustic power i.e. 10^{-12} W [32].

5. Methodology

In this chapter, the procedure followed to create the CAD geometry of the blade, meshing and CFD simulations is first outlined. The procedure outlined below is by taking the 7m/s inlet velocity operating condition as an example. The same procedure has been followed for three other wind operating conditions namely 10m/s, 13m/s and 15m/s.

Once the flow field information through CFD analysis is obtained for the four wind operating conditions mentioned above, the set up pertaining to aeroacoustics is then outlined.

5.1 STAR CCM+

STAR CCM+ is a comprehensive physics simulator that has been developed by CD-Adapco. Flow simulation is one among the many simulations that can be performed using STAR CCM+. CAD modelling, meshing, CFD analysis and aero-acoustic analysis can be performed using the same software package which helps avoid the need to import CAD files or mesh files created using other CAD or meshing packages and thus we encounter less to no surface repair issues due to the difference in tolerances set up in different software packages which makes it more convenient to use as opposed to other CFD packages.

Flow simulations can be performed using either coupled flow solver that is typically used for high Mach number flow conditions or segregated flow solver that is used for low flow speed conditions. The solver also offers a variety of turbulence models as a choice for simulations with many of them having three different enhanced wall treatment conditions namely the low y+ wall treatment when $y+<1$, high y+ wall treatment when $y+>30$ and all y+ wall treatment.

STAR CCM+ also performs aero-acoustic analysis using the predicted CFD results. There are number of aero-acoustic models present in STAR CCM+ which helps in predicting noise either using steady state results or using unsteady state results based on the case at hand.

For the simulations performed in this computational study, the CAD model, meshing, CFD analysis and aero-acoustic analysis has been performed using STAR CCM+.

5.2 3 D CFD analysis of the NREL Phase VI blade

The flow across a wind turbine rotor is inherently three dimensional in nature. The flow separation first begins at the root of the blade and this gradually moves towards the tip. This occurs because of centrifugal acceleration and pressure gradients present in the radial direction.

The wind that has been separated at the blade root, flows in the radial direction. This wind flow forcibly generates a 3-D flow separation along the blade surface [13].

To take this phenomenon into account and to make a more realistic prediction of the flow field around a wind turbine a 3 D flow simulation has been performed.

The NREL Phase VI rotor has a diameter of 10.058m and rotates with a speed of 72 rpm in the counter clockwise direction when viewed from upstream of the rotor. The S-809 airfoil has been used to create the blade geometry. Other additional information pertaining to blade geometry has been outlined earlier in the literature review.

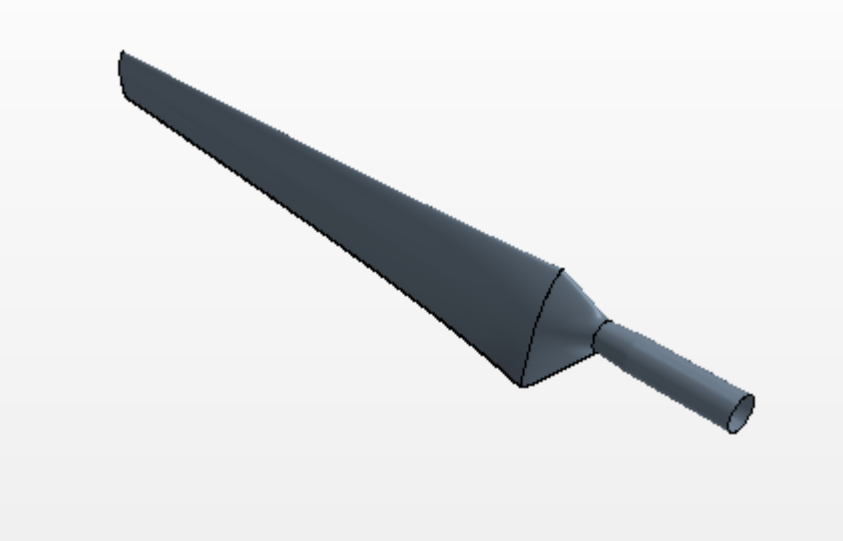

Figure 22: CAD model of blade geometry

Since blockage effects due to the presence of wind tunnel walls are negligible a cylindrical domain is chosen for our simulation [21]. The choice of cylindrical domain helps in implementing the rotational reference frame. According to this, the blade is considered to be stationary and the flow field that is incident on the rotor rotates as it impinges on the blade. With this assumption, an unsteady flow field turns into a steady state flow [12]. Through this assumption, it is possible to avoid the usage of sliding meshes which saves computational time and still yield accurate CFD results.

In addition to this, with the usage of the rotational periodic boundary, it was possible to simulate only one blade that is placed in a semi-cylinder instead of two blades due to the rotational symmetry that is present in this NREL Phase VI rotor that contains two blades that are 180^0 apart. The advantage of using this rotational periodic boundary condition, the mesh size was reduced to half its original size which once again brought down its computational costs. It must be noted that while implementing the rotational periodic boundary on to the two

periodic surfaces, the mesh has to be generated such that that they are mirror images of each other.

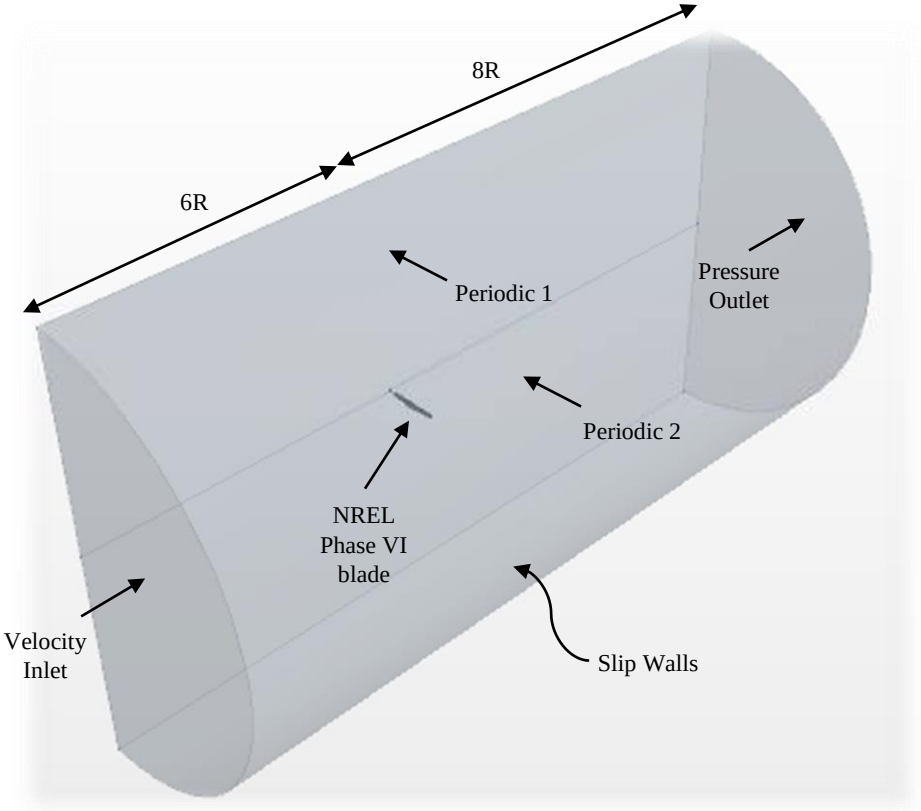

Figure 23: Semi-Cylindrical domain containing NREL Phase VI Blade.

5.2.1 Polyhedral Mesh

An unstructured polyhedral mesh along with prism layers has been used to create the required mesh. The polyhedral mesher present in STAR CCM+ is very robust and is capable of creating automatic mesh with the specifications of surface element sizes and curve elements size which are used to capture the shape and curvature of the given geometry accurately. Polyhedral meshes are found to be superior to tetrahedral meshes since each cell in a polyhedral mesh has typically about 10 neighbors and thus it is possible to obtain greater accuracy using these meshes as greater number of neighbors implies greater storage and thus greater computing

operations. Polyhedral meshes have proved to be robust in cases involving external aerodynamics and is well suited for this simulation.

In this case a polyhedral mesher has been utilized to create a semi-cylinder that contains the wind turbine blade as shown below. The velocity inlet has been placed six times the rotor radius upstream of the rotor and the pressure outlet has been placed eight times the rotor radius downstream of the rotor.

5.2.2 Mesh Set up

The mesh set up outlined in this section is associated with polyhedral volume mesh and surface remesher settings. The base surface size chosen for meshing is 0.01m and on the tip of this blade 12% of this size is chosen for these elements. Every other part of the blade has a surface size that is 100% of the chosen base size. All surfaces of the domain namely velocity inlet, pressure outlet, slip wall and the two periodic surfaces are chosen to have a 2m size for their elements. The curve elements along the leading edge are having a size of 8% of the base size and the trailing edge surface has 3% of the base size. The surface growth rate of 1.3 has been used while creating this mesh.

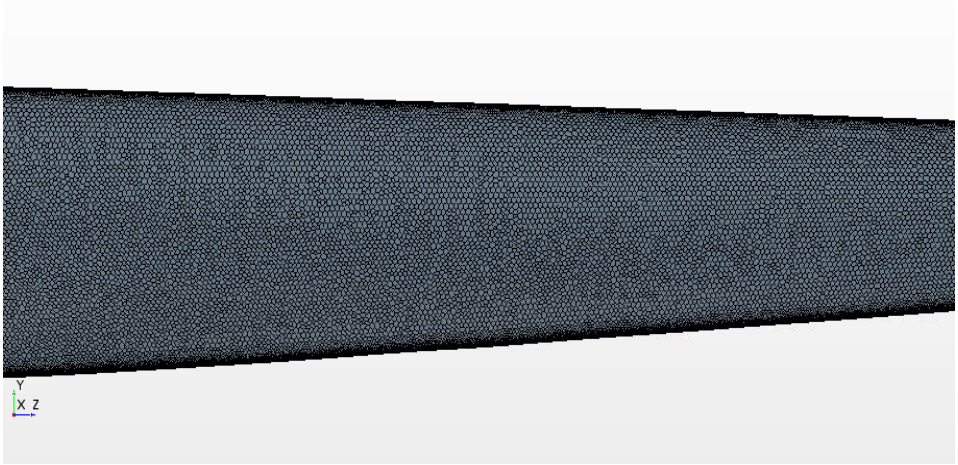

Figure 24: Mesh generated on blade surface

In addition to this, there are two refinement regions that have been included to ensure slow growth rate of volume mesh. The first refinement region is immediately surrounding the blade as shown in the figure below. In this region, the size of cells corresponding to both the surface remesher and volume mesh are of 0.03m.

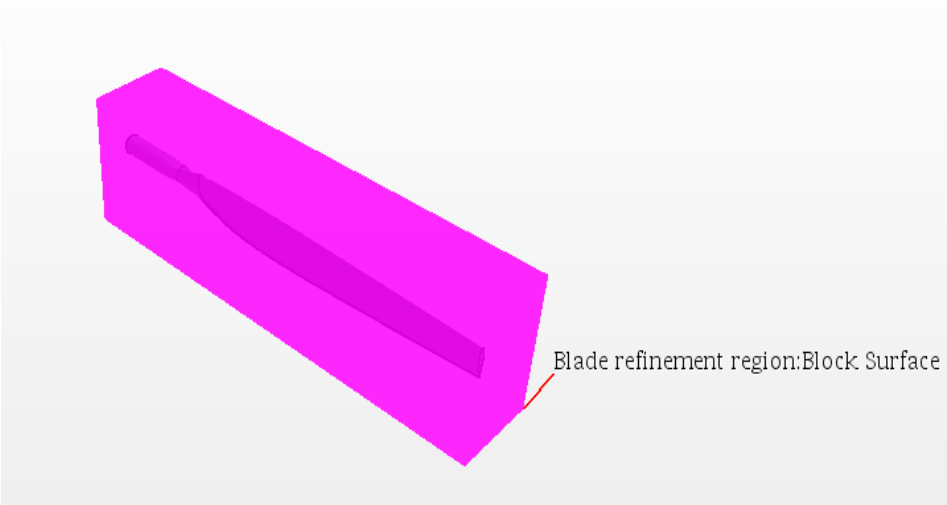

Figure 25: Blade refinement region

The second refinement region is cylindrical density region which surrounds the entire blade span. The radius of this cylinder is 6m and is 3m thick with 1m thickness present upstream of the rotor and the 2m thickness present downstream of the rotor. The element size during both surface remesher and volume mesh operation is specified to be 0.6m in this region.

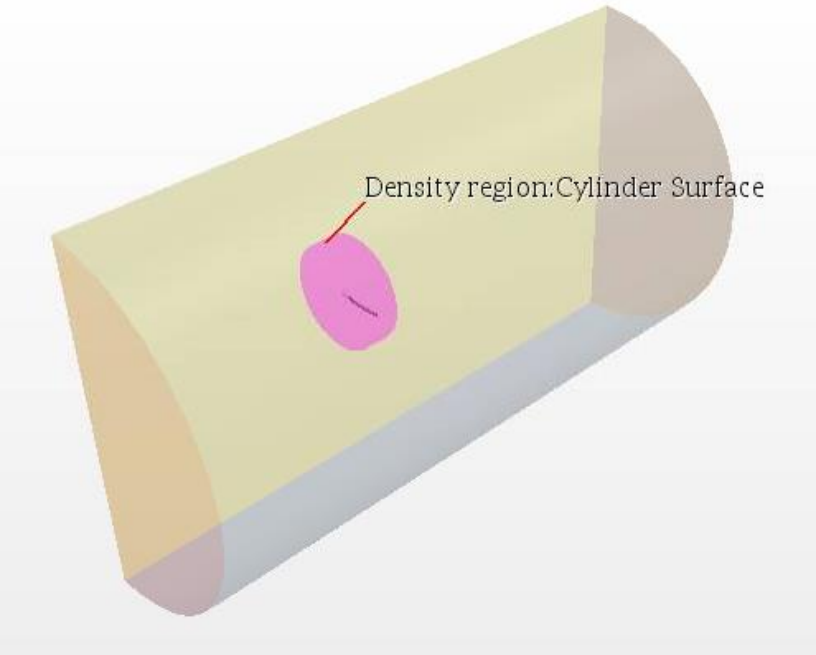

Figure 26: Density region around the blade surface

5.2.3 Modifying the blade trailing edge

The S-809 airfoil that has been used to create the blade geometry is such that using the exact coordinates of this blade leads to the formation of a sharp trailing edge. The drawback of using a sharp trailing edge is that the prism layers formed along this sharp edge leads very poor quality elements. Furthermore it is unrealistic to have a sharp trailing edge which would lead to structural failure of a blade and thus requires some extent of bluntness. For this reason, the chord length of the blade was reduced by 2% along the trailing edge and a suitable fillet was provided in this region. This was achieved by altering the existing coordinates of the S-809 airfoil in the trailing edge region.

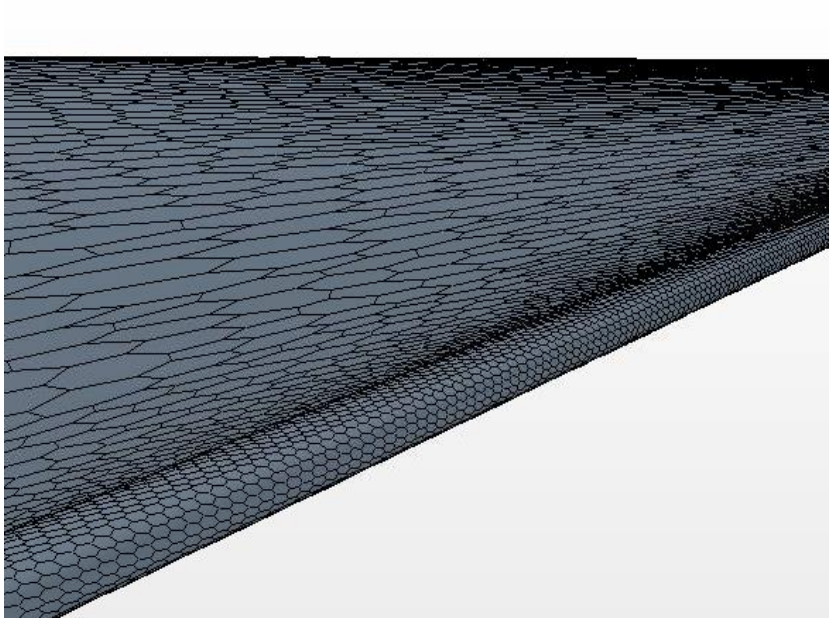

Figure 27: Blunt Trailing edge created along the blade span

The variation of chord based Reynolds number at root, mid span and tip of the blade for 7m/s, 10m/s, 13m/s and 15m/s have been represented in the graph below.

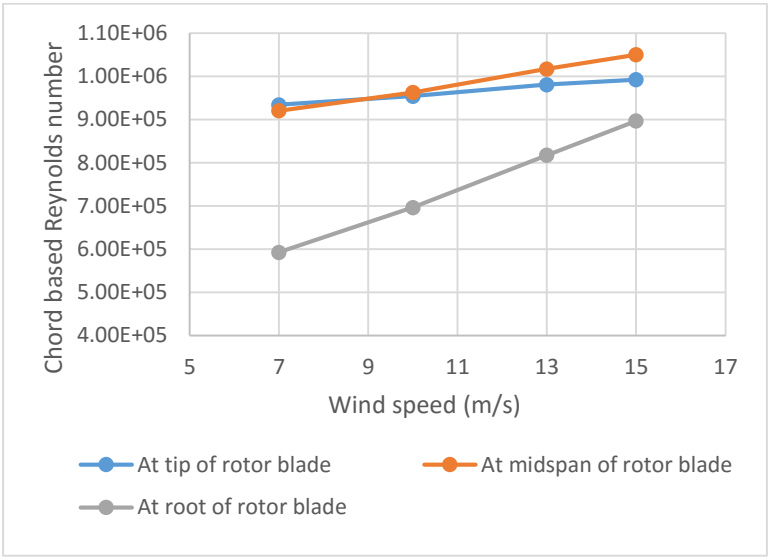

Figure 28: Plot of Reynolds number based on chord versus wind speeds at three span locations of the blade

We see that the Reynolds number based on chord varies from around 600,000 at blade root to to 940,000 at blade tip for 7m/s and from 897,000 to 993,000 for 15m/s. Since SST k-ω turbulence model is used for CFD analysis, a y+ value of less than 5 was created with the intention of keeping the prism layers to fall in the viscous laminar sub layer.

A prism layer thickness of 0.0065m was created using 20 prism layers and a growth ratio of 1.3. Finally the mesh generated had about 10.2 million cells.

5.2.4 Initial and Boundary conditions

All surfaces of the blade geometry was left as default no-slip wall boundaries. The surface of the domain perpendicular to the direction of inlet flow direction that is present upstream of the rotor is designated as velocity inlet. The surface of the domain perpendicular to the flow direction present downstream of the rotor is designated as pressure outlet. The curved surface of the domain is considered as slip walls and the two surfaces which makes contact with the blade as shown in the figure below are designated as rotational periodic boundaries.

An inlet velocity of 7m/s was specified on the velocity inlet boundary and the turbulence viscosity ratio was specified as 0.5 [23]. Since the reference pressure in the initial conditions was specified as the ambient pressure that was provided by experimental data [21], the gauge pressure at the pressure outlet boundary condition was specified to be 0 Pa. A rotational reference frame was created such that the blade rotates with an angular velocity of 7.54 rad/s in the counter clockwise direction.

The various CFD and mesh settings that have been used for this simulation has been outlined below

Input Variable	**Setting**
Flow type	Three dimensional
Time dependence	Steady
Equation of state	Constant Density
Flow solver	Segregated flow solver
Viscous regime	Turbulent
Reynolds average turbulence	k-ω turbulence
Enhanced wall treatment	All y+ wall treatment
y+	Less than 5
Mesh	Unstructured- Polyhedral

Table3: Mesh and CFD settings

The same set up and mesh created was used for other wind operating conditions also.

5.2.5 Aeroaocustic simulation set up

Firstly, the flow field data is to be obtained through CFD analysis using the set up conditions outlined previously. To ensure that the flow field has been predicted accurately, certain performance characteristics and aerodynamic characteristics such as torque generated by the NREL Phase VI rotor and the trends of pressure coefficients at different span locations are validated against both experimental results and results from previous computational studies on this case. Once this validation is completed, the flow field data that has been predicted accurately using Reynolds averaged Navier Stokes equations is utilized to predict the noise sources on the blade surface. The Curle broadband noise source model has been chosen for this purpose. This model can be chosen from Physics Models option through the steps outlined below.

Input Variable	Setting
Aeroacoustic Model	Broadband noise sources
Noise Source model	Curle

Table 4: Aeroacoustic settings

6. Results and Discussions

This section has been divided into two parts. The first part presents results pertaining to aerodynamic and performance characteristics of the NREL Phase VI wind turbine rotor. This has been done to validate the prediction of flow field results through CFD analysis. The second part presents the distribution of aerodynamic noise sources across the blade surface at different wind operating conditions.

6.1 Trends of Pressure Coefficients at different span locations of the blade

The trends of pressure coefficients at different sections of the blade that has been obtained through steady state CFD analysis using the SST k-ω turbulence model is compared with the corresponding time averaged pressure coefficient trends obtained through experimental analysis on the NREL Phase VI blade. There were number of pressure taps that were placed along the airfoil sections at 30%, 46.6%,63.3%, 80% and 95% of the blade span [21]. The static pressure on the blade was measured using these pressure taps for 30 seconds time period. These static pressures were then non-dimensionalized using dynamic pressure to obtain pressure coefficients at the given locations.

6.1.1. At Wind speed of 7m/s

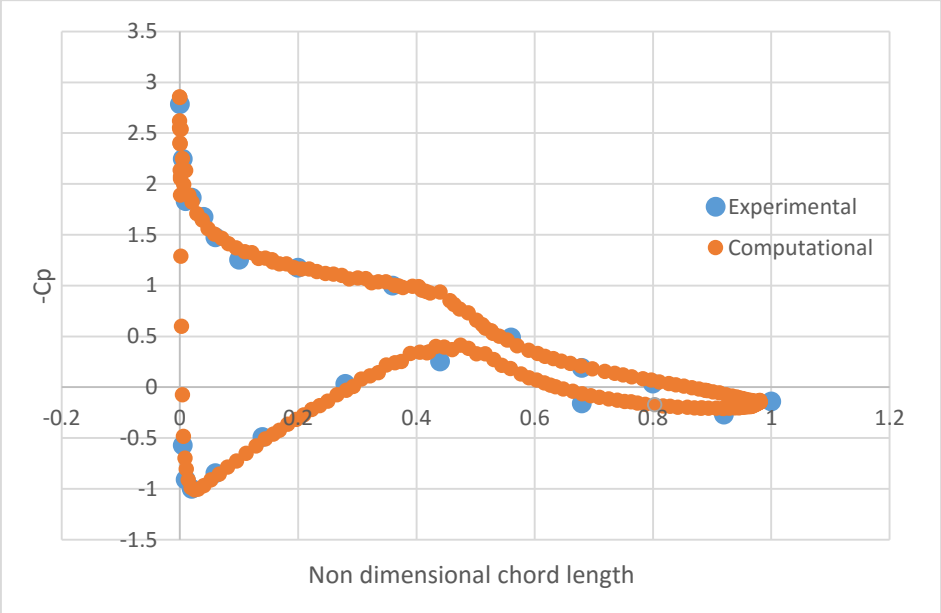

Figure 29: Pressure coefficient comparison at 30% blade span for 7m/s

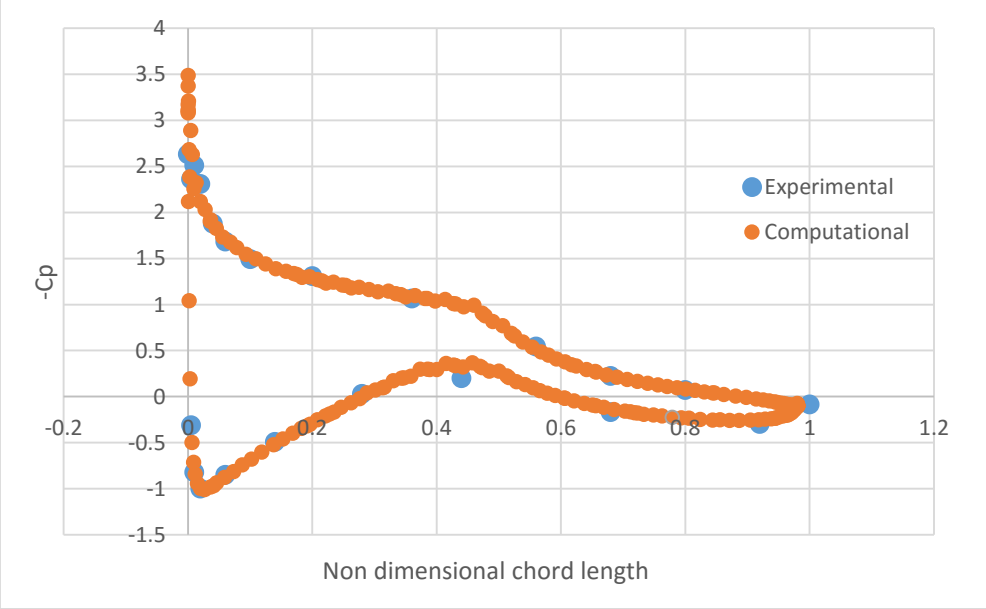

Figure 30: Pressure coefficient comparison at 46.6% blade span for 7m/s

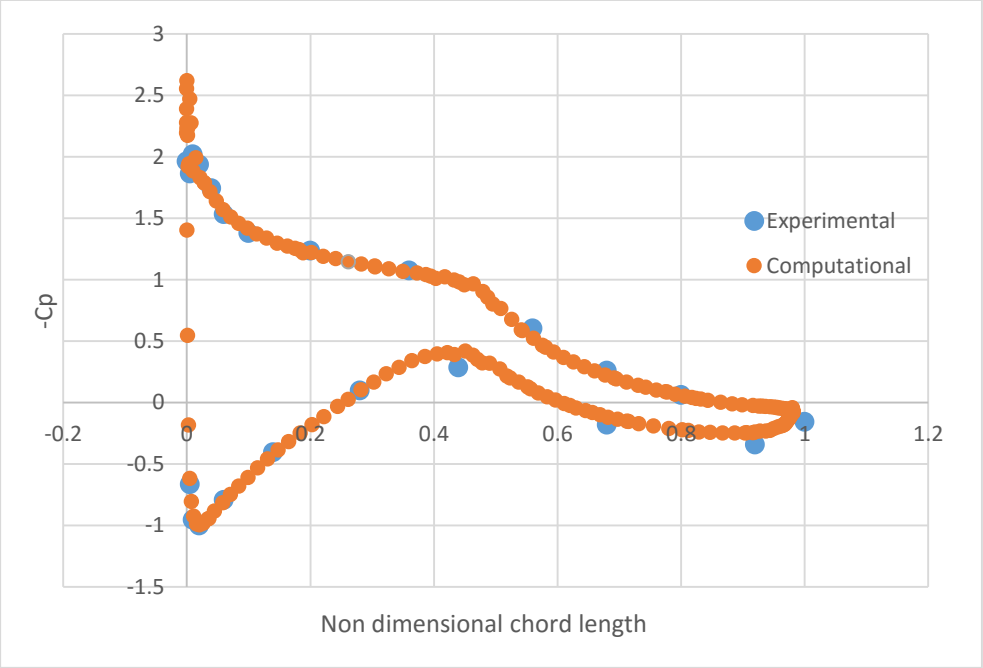

Figure 31: Pressure coefficient comparison at 63.3% blade span for 7m/s

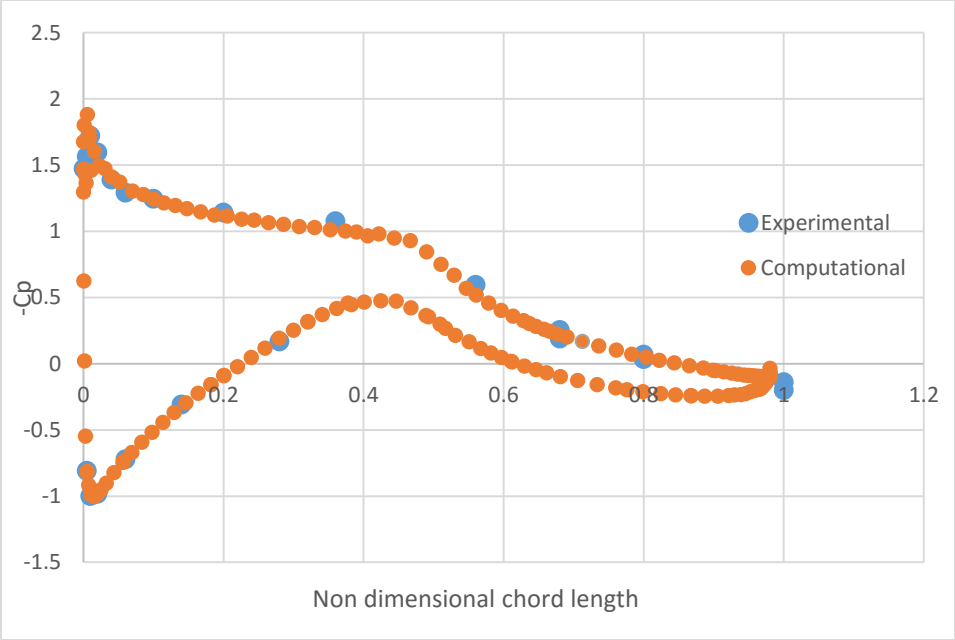

Figure 32: Pressure coefficient comparison at 80% blade span for 7m/s

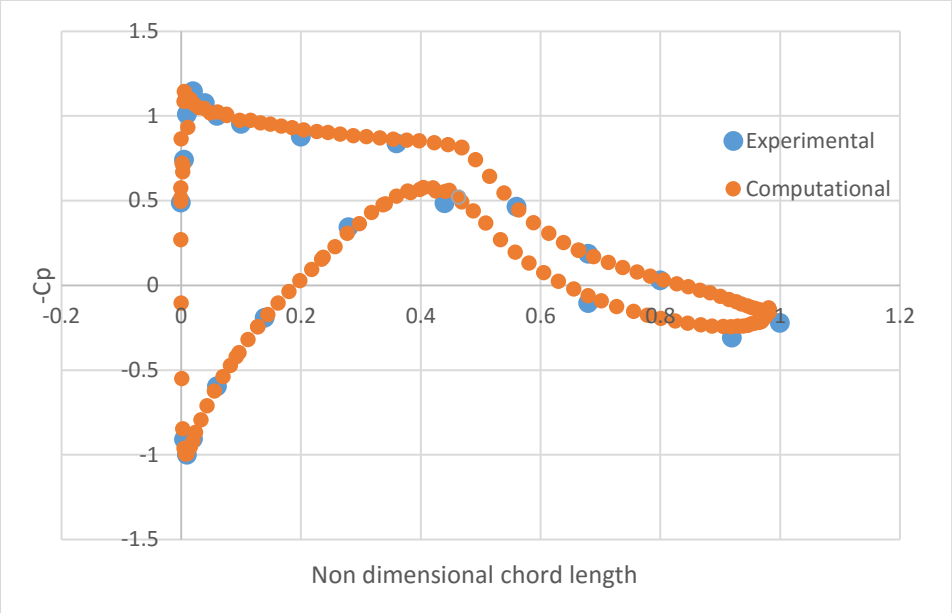

Figure 33: Pressure coefficient comparison at 95% blade span for 7m/s

From the above plots, we see that that trends of pressure coefficients predicted through CFD analysis show good agreement with the experimental trends of pressure coefficients for a wind speed of 7m/s. The accuracy in these results are expected at this wind speed because at low wind speeds such at 7m/s, the flow remains attached along the blade span except in a small region near the root of the blade and the SST k-ω model is a good predictor of CFD flow filed in cases where flow separation is minimal. We also see that the trends of pressure coefficients is accurate particularly near the leading edge and near the trailing edge of the blade for each of the given airfoil sections.

6.1.2. At wind speeds of 10m/s

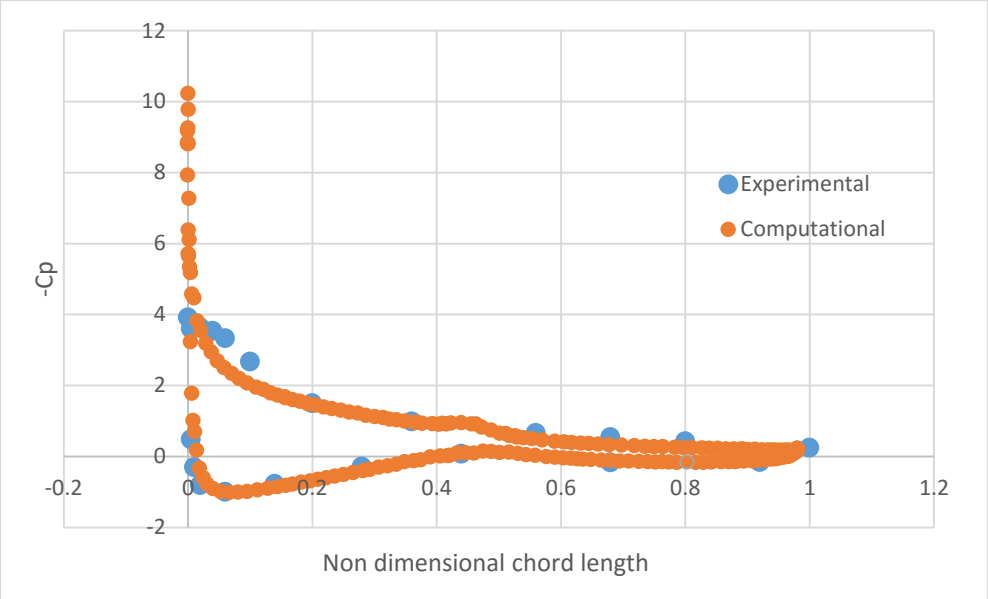

Figure 34: Pressure coefficient comparison at 30% blade span for 10m/s

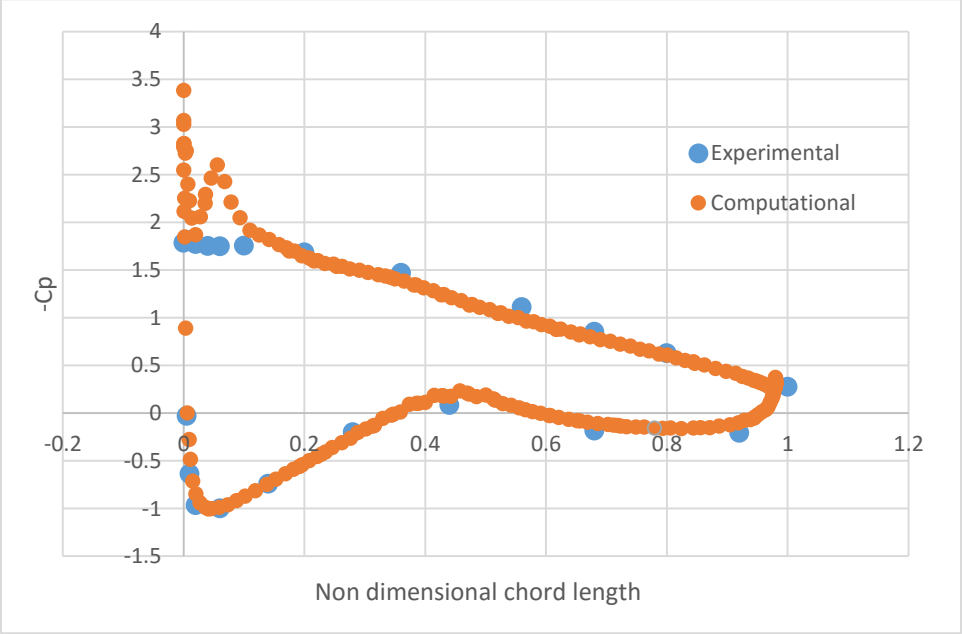

Figure 35: Pressure coefficient comparison at 46.6% blade span for 10m/s

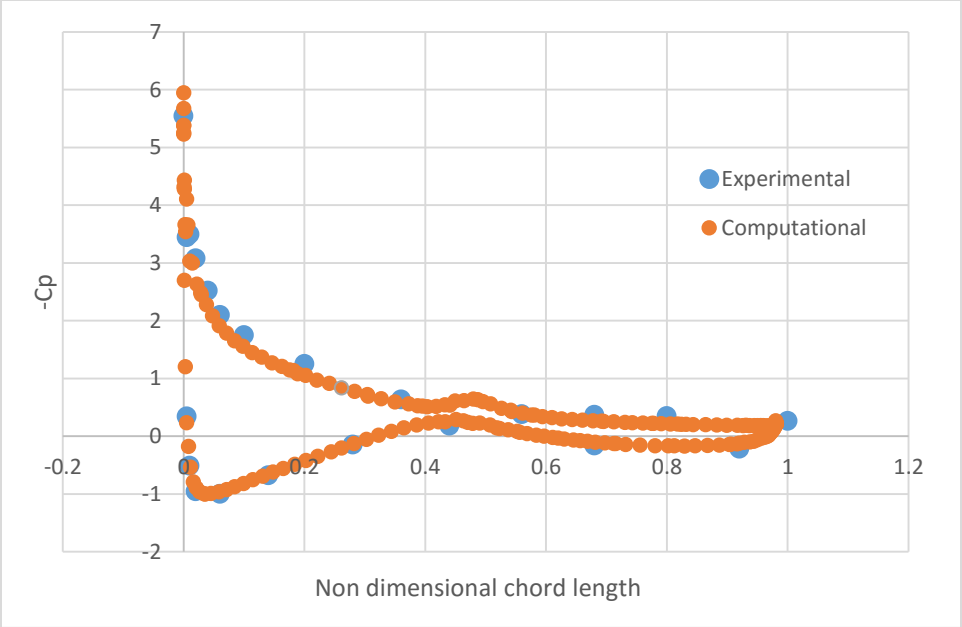

Figure 36: Pressure coefficient comparison at 63.3% blade span for 7m/s

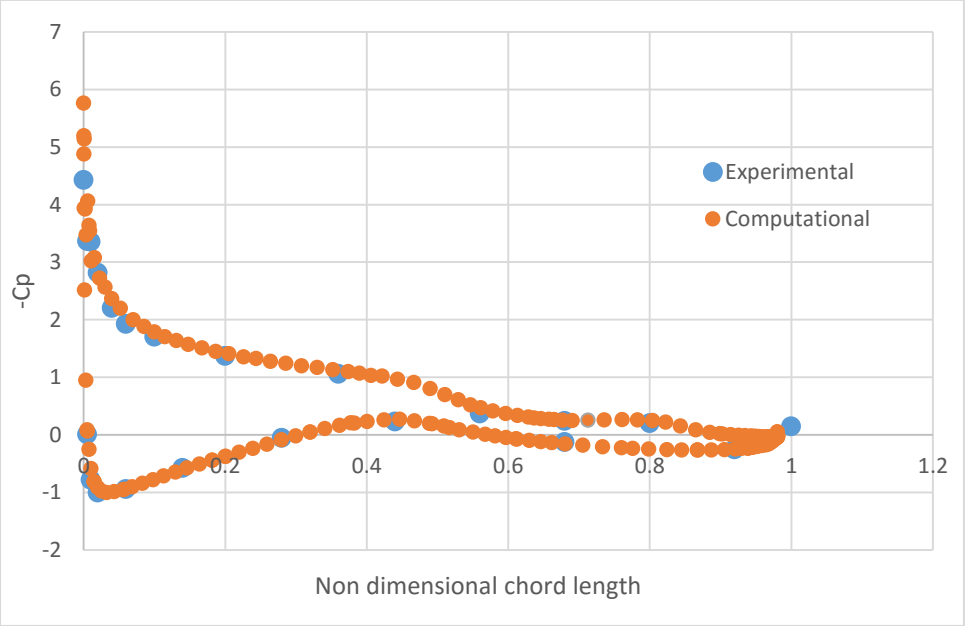

Figure 37: Pressure coefficient comparison at 80% blade span for 10m/s

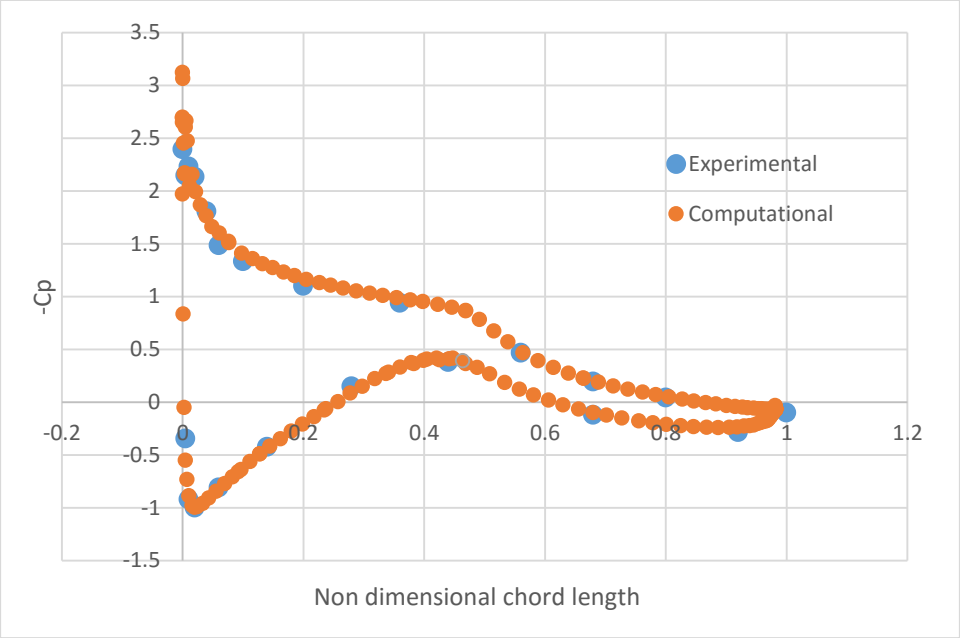

Figure 38: Pressure coefficient comparison at 95% blade span for 10m/s

From the above plots for 10m/s, we see that trends of pressure coefficients that has been predicted for span locations of 30% and 46.6% of blade span has not been predicted accurately. This discrepancy is observed especially near the leading edge of the section of the blade where the computational results indicate a sharp peak in the predicted pressure coefficients on the suction side. However, this is not unique to this computational study and such a trend has also been observed in other CFD analysis for the same case [14, 15]. This discrepancy has been attributed to separation of flow in these regions. We also observe that the trends of pressure coefficients have been accurately predicted near the trailing edge of the blade for these two sections.

Sections 63.3%, 80% and 95% of blade span show good agreement with the experimental trends of pressure coefficients for this wind speed of 10m/s.

6.1.3. At wind speed of 13m/s

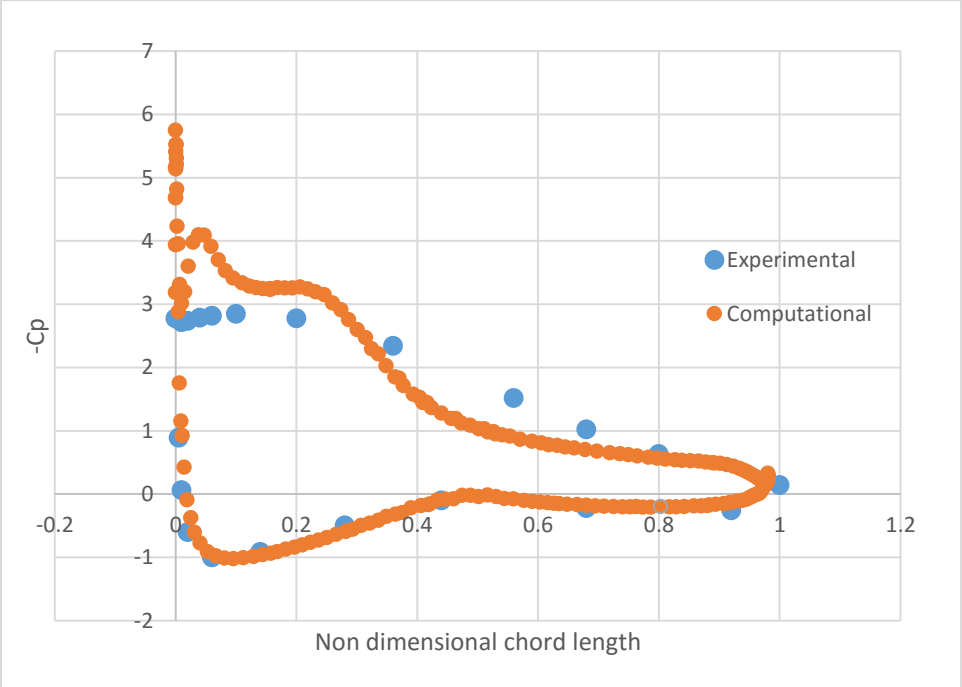

Figure 39: Pressure coefficient comparison at 30% blade span for 13m/s

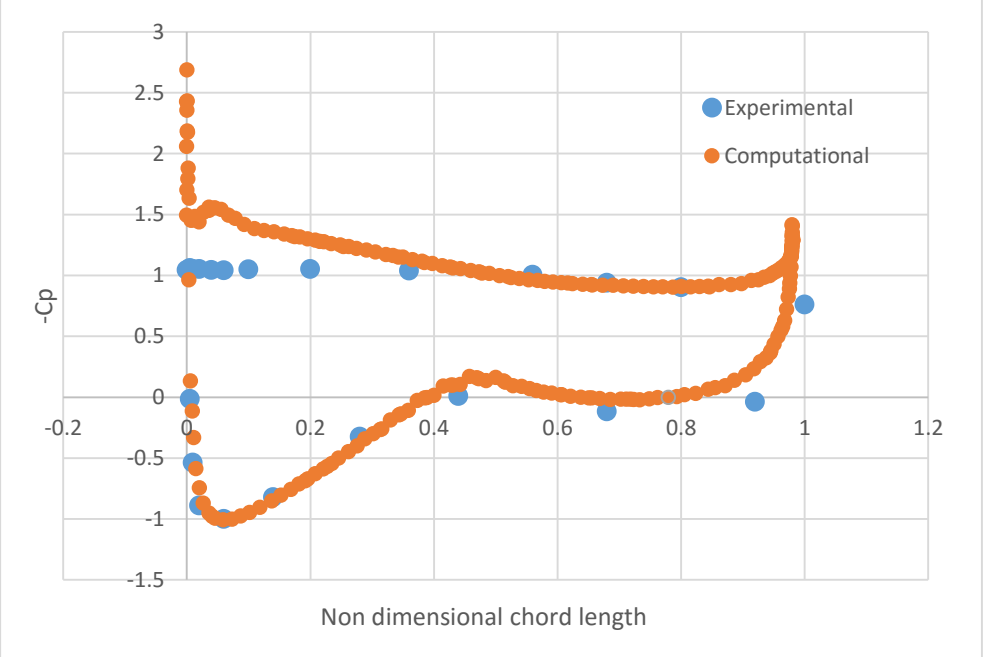

Figure 40: Pressure coefficient comparison at 46.6% blade span for 13m/s

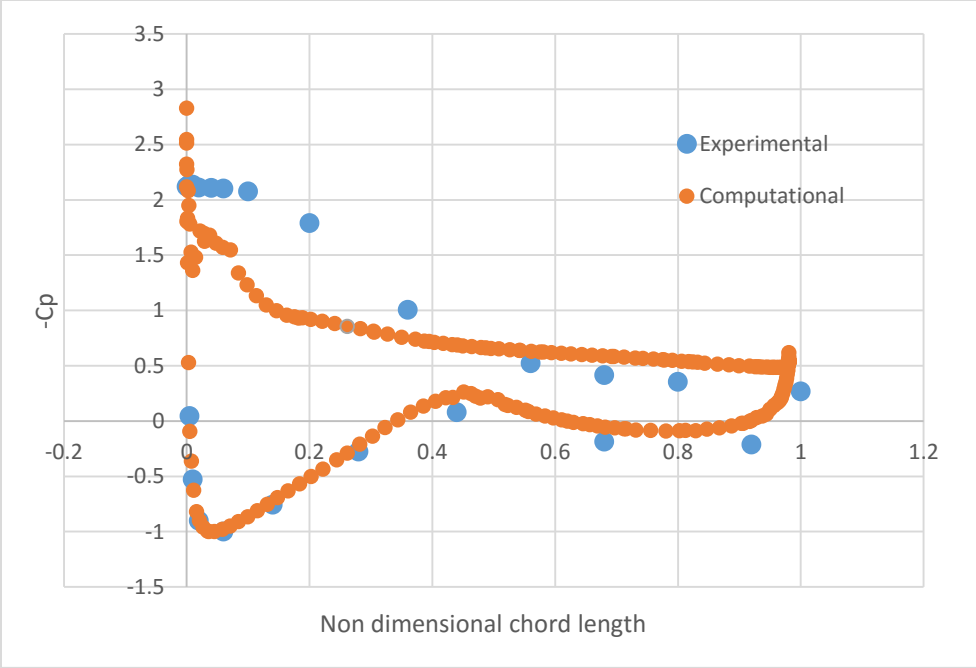

Figure 41: Pressure coefficient comparison at 63.3% blade span for 13m/s

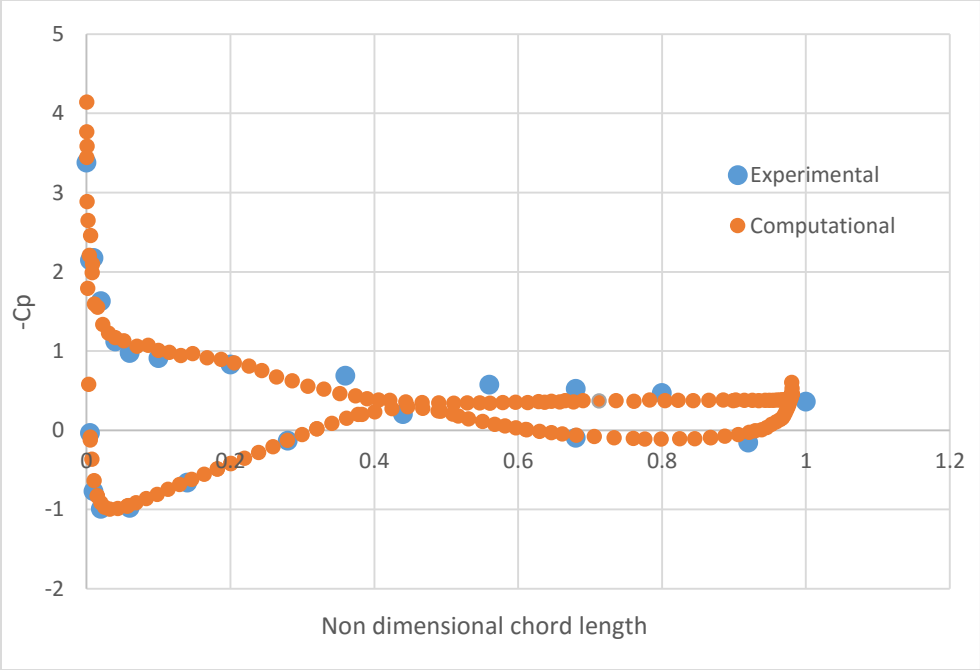

Figure 42: Pressure coefficient comparison at 80% blade span for 13m/s

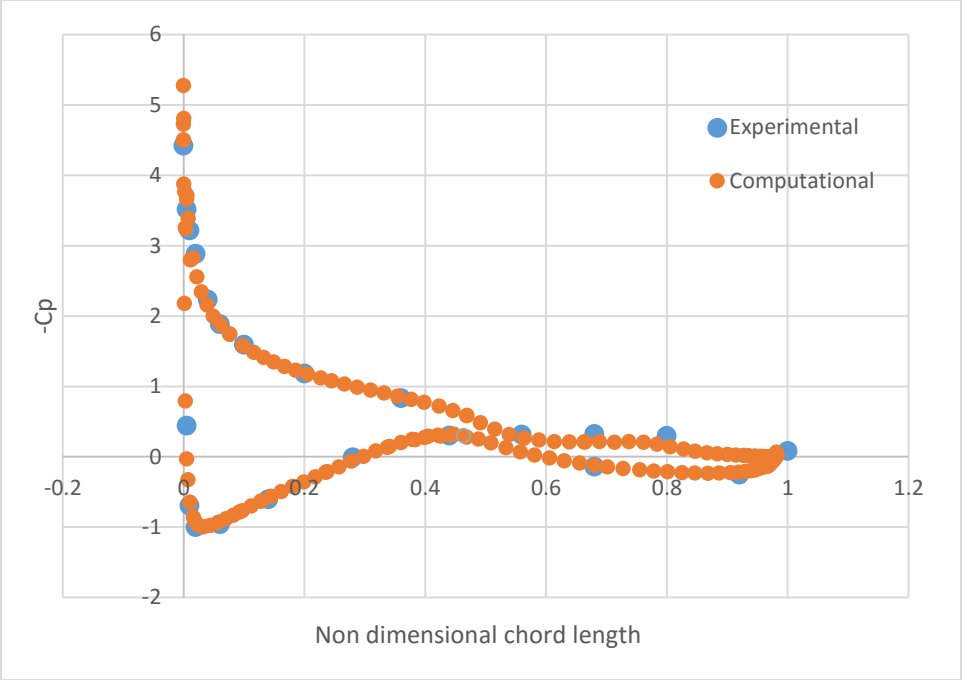

Figure 43: Pressure coefficient comparison at 95% blade span for 13m/s

For a wind speed of 13m/s, we see that the accuracy of trends of pressure coefficients predicted near the leading edge of the blade for sections 30% and 46.6% and 63.3% is quite low as compared to the case of 7m/s. However the trend in pressure coefficients predicted in the remaining regions are accurate. We also observe that the pressure coefficients predicted at sections corresponding to 80% and 95% of blade span shows good agreement with the experimental results. The inaccuracy in the results predicted in former regions can once again be attributed to flow separation and the inability of SST k-ω turbulence model to predict the flow field accurately in regions that experience the same.

6.1.4. <u>At wind speed of 15m/s</u>

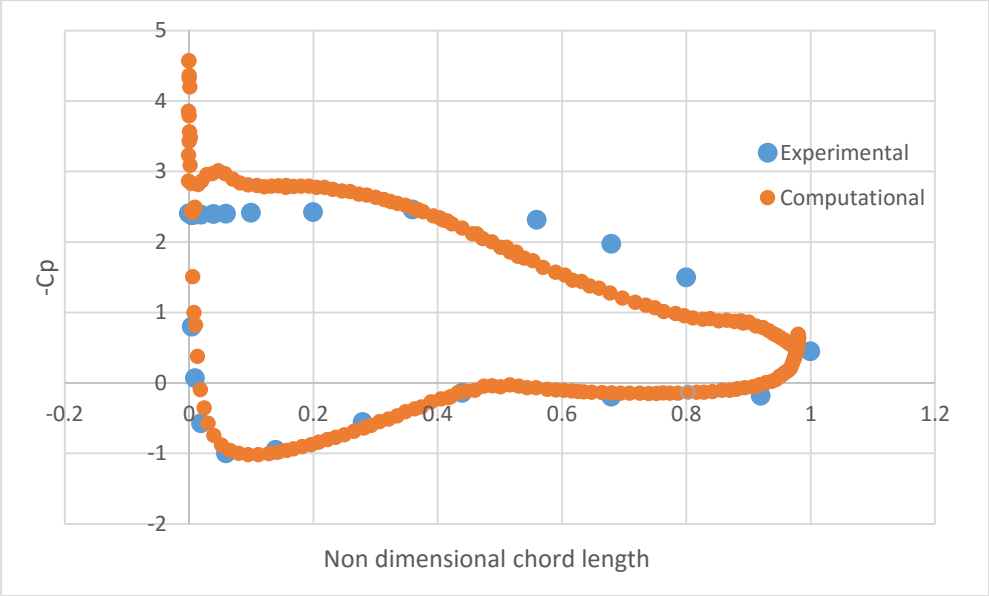

Figure 44: Pressure coefficient comparison at 30% blade span for 15m/s

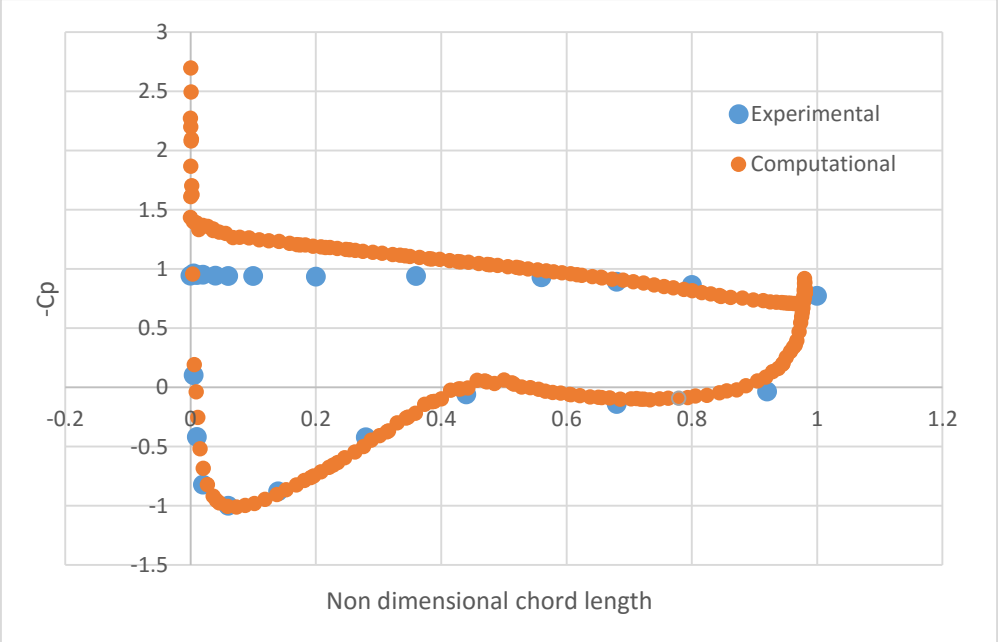

Figure 45: Pressure coefficient comparison at 46.6% blade span for 15m/s

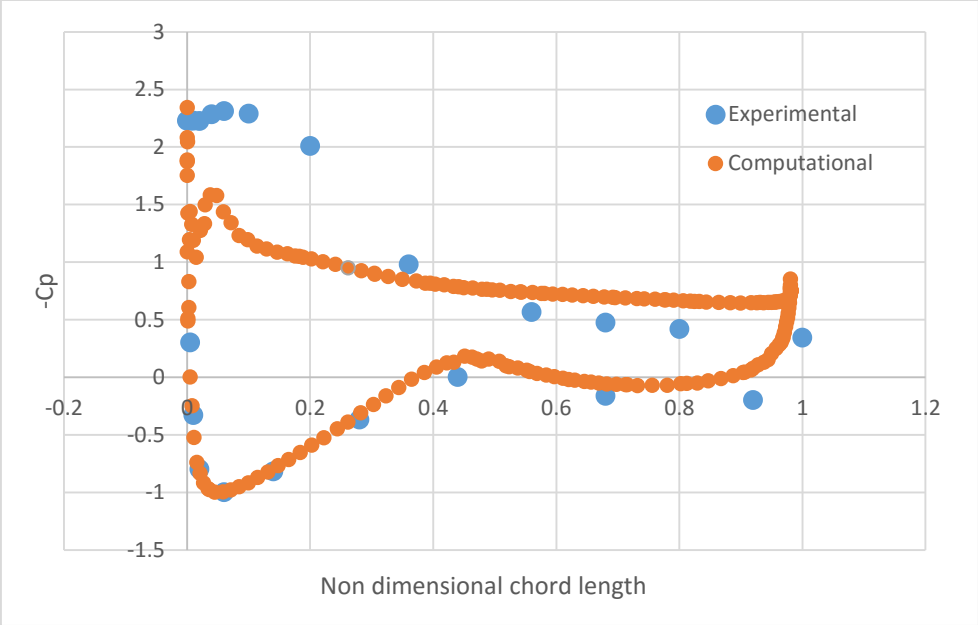

Figure 46: Pressure coefficient comparison at 63.3% blade span for 15m/s

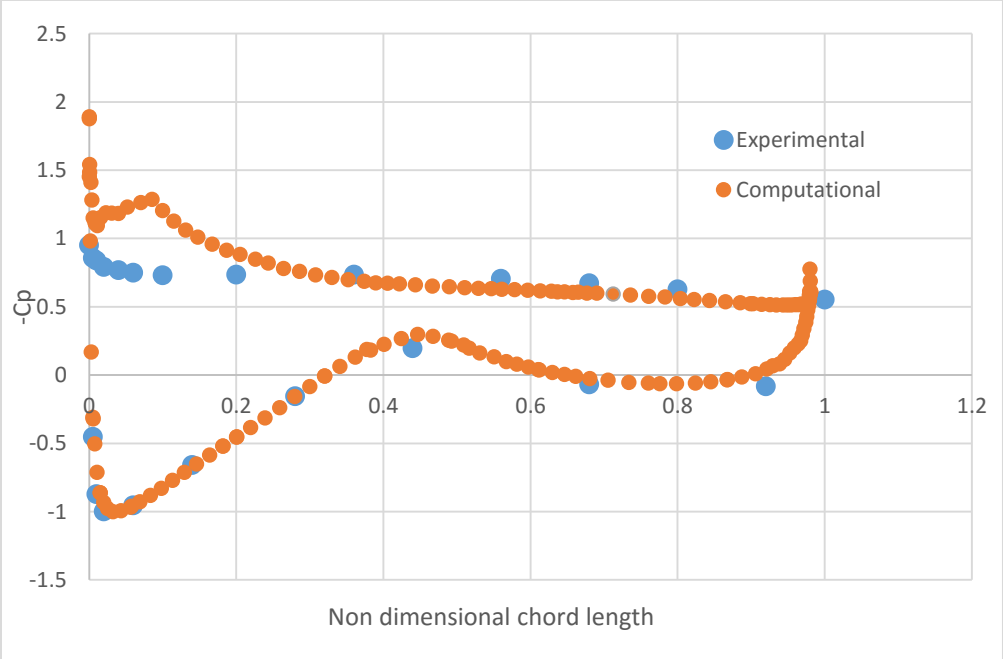

Figure 47: Pressure coefficient comparison at 80% blade span for 15m/s

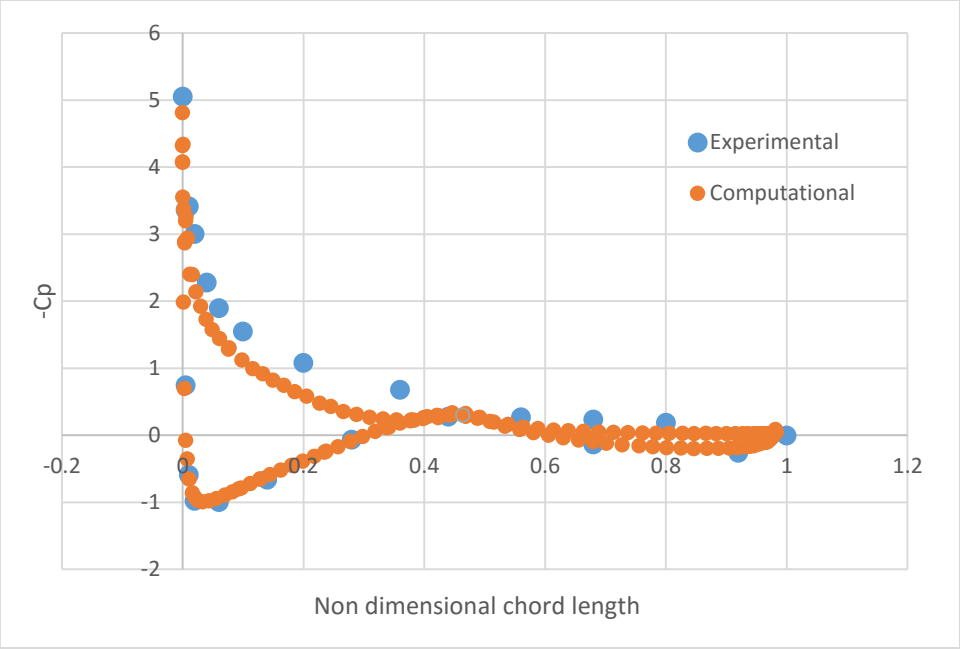

Figure 48: Pressure coefficient comparison at 95% blade span for 15m/s

For a wind speed of 15m/s, we see that apart from the section located at 63.3% blade span where the pressure coefficients near the leading edge on the suction side is under predicted, the results observed at all other sections of the blade span show reasonably good agreement with the experimental results, especially considering the high wind speed. As observed in previous cases, we see a sharp peak near the leading edge of the blade on its suction side which is prominent in case of 30% and 46.6% blade span locations. However, since this trend was also observed in previous computational studies, we can consider the computational predictions of trends of pressure coefficients for this case also to be acceptable.

6.2 Prediction of Torque generated by NREL Phase VI rotor

While performing steady state CFD analysis, torque coefficient was monitored in addition to the residuals of conservation of mass, momentum, energy, turbulent kinetic energy and turbulent dissipation rate for its accurate convergence. The torque coefficient obtained through simulation was for only one rotor blade (using the rotational periodic boundary). The torque generated by the two blades was found using:

$$T = nC_T\left(\frac{1}{2}\rho_\infty V_\infty^2 SL\right) \tag{6.1}$$

where,

T is the net torque generated by wind turbine rotor having "n" number of blades

ρ_∞ is the density of ambient air

V_∞ is the inlet velocity

S is the planform area of the blade

L is the span of the blade

C_T is the torque coefficient

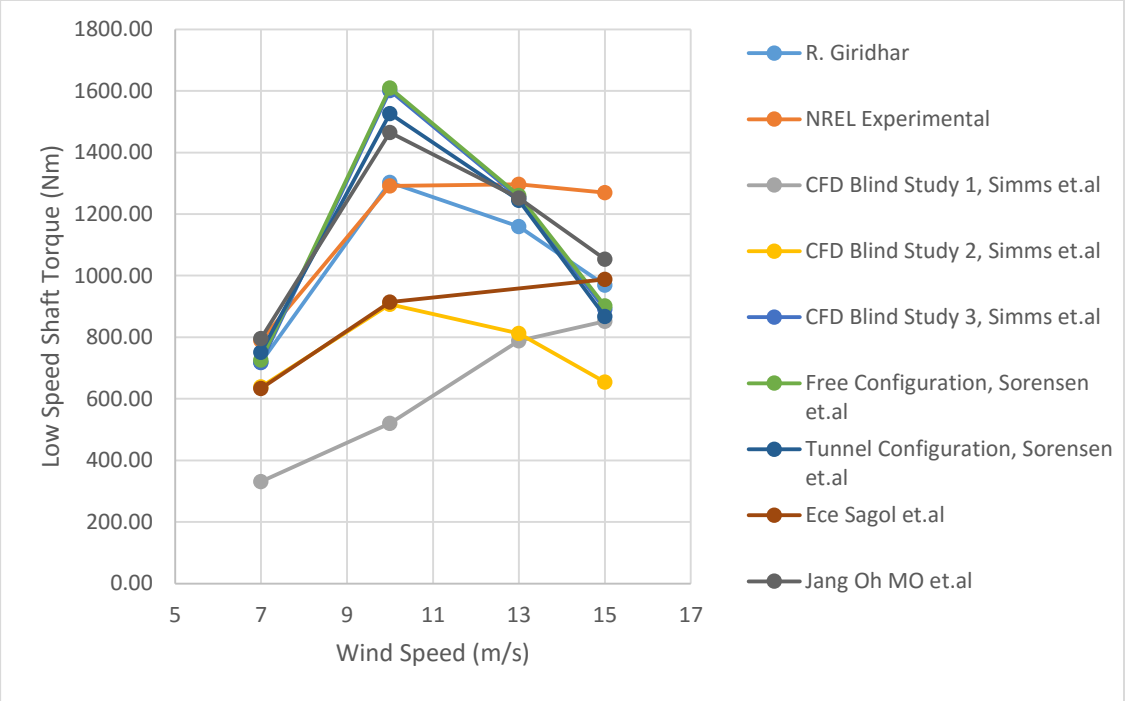

Figure 49: Comparison of torque prediction

It is observed that the torque predicted by this computational study shows good agreement with the experimental torque especially at 7m/s and 10m/s and 13m/s wind speeds. It is seen that for wind speed 15m/s, the torque has been under-predicted when compared to the experimental torque.

It is also observed that the torque predicted by previous computational studies show the same trend as is predicted through this simulation and they too under predict the torque at wind speeds of 13m/s and 15m/s. The torque predicted at 7m/s and 13m/s have an error of about 10% whereas the torque predicted at 10m/s has an error of only 0.8%. This computational study has under predicted the torque at 15m/s by 20% when compared to the experimental torque. In general, we see that the torque predicted by this computational study shows good agreement when compared to experimental torque and when compared to previous computational studies.

6.3 Prediction of noise sources at different wind speeds

Now that the aerodynamic characteristics and performance characteristics obtained through CFD analysis of the NREL Phase VI rotor shows good agreement with experimental studies, we can conclude that the flow field predicted by the SST k-ω turbulence model for the four wind speed conditions are accurate and can be used to perform aero acoustic prediction to determine the location and magnitude of the major noise sources present on the blade surface. This aeroacoustic prediction was performed using Curle broadband noise source model.

6.3.1 At Wind speed of 7m/s

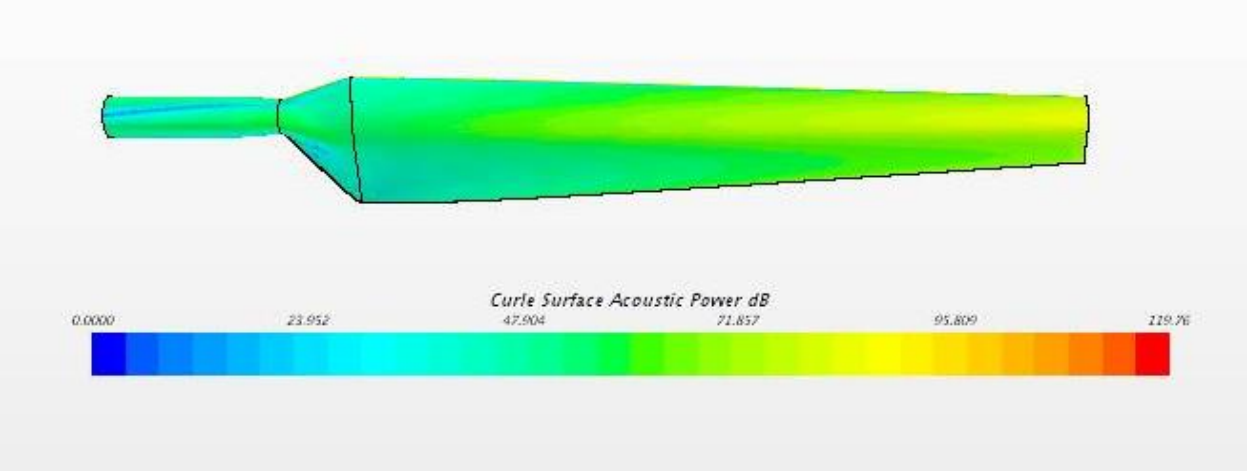

Figure 50: Sound Power Level distribution of noise sources on pressure surface of blade at 7m/s.

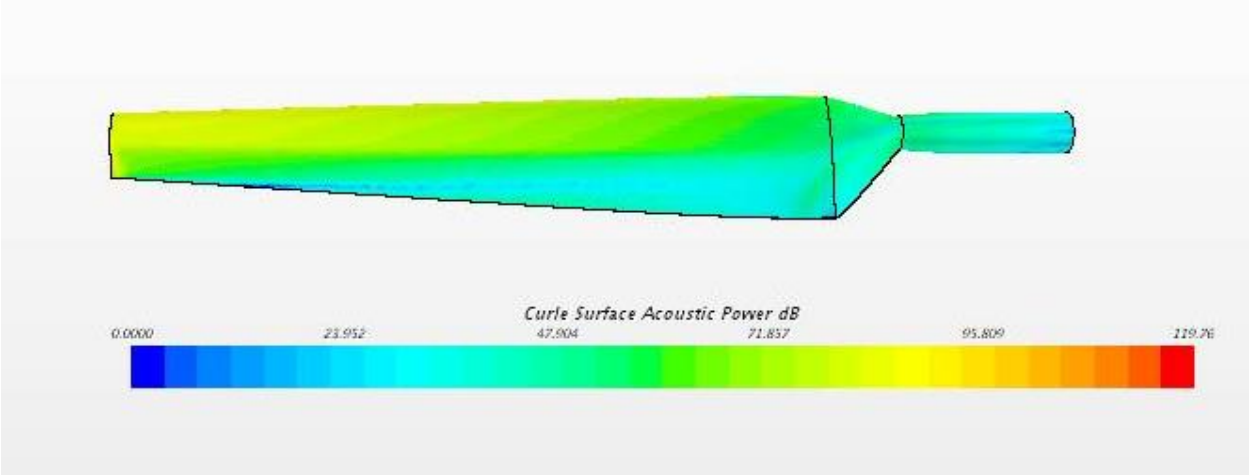

Figure 51: Sound Power Level distribution of noise sources on suction surface of blade at 7m/s.

Based on the scalar field of Sound Power Level distributions that we see above for 7m/s wind speed, we see that the major noise sources are located near the tip of the blade. The intensity of noise generated by the sources decreases as we move along the span of the blade from tip to its root. We see that about half region of the blade has an average sound power level of about 40dB and the other half region of the blade has average sound power level of about 65dB.

6.3.2 <u>At Wind speed of 10m/s</u>

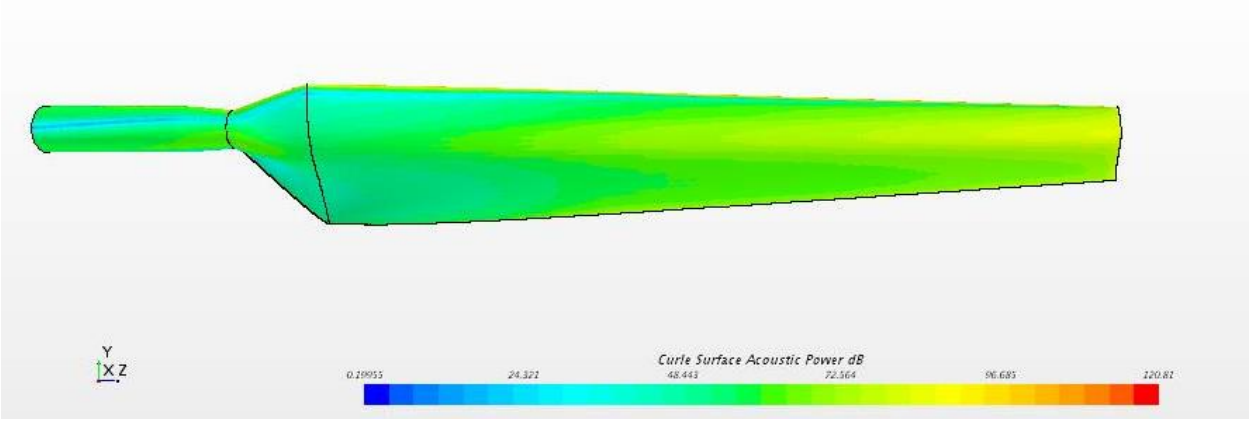

Figure 52: Sound Power Level distribution of noise sources on pressure surface of blade at 10m/s.

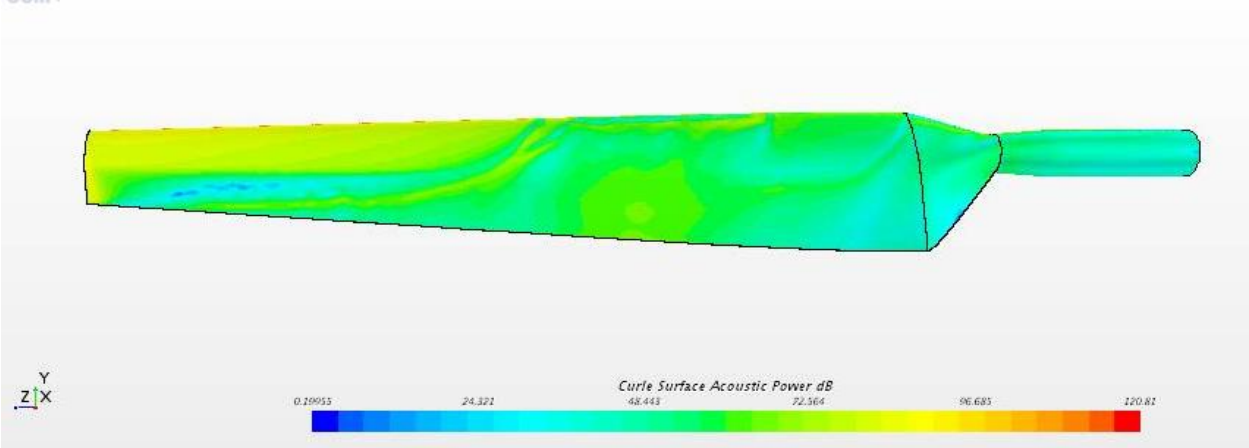

Figure 53: Sound Power Level distribution of noise sources on suction surface of blade at 10m/s.

For wind speed of 10m/s, we see that the Sound Power levels of noise sources are slightly greater near the tip as compared to the case of 7m/s. This can be observed on both suction and pressure surfaces of the blade. It is observed that the sound power level distribution on the suction side of the blade does not have a uniform distribution as seen on the pressure side of the blade in the mid-span region. This could be attributed to the poor flow field prediction in this region which was also observed while predicting the trends of pressure coefficients on the suction side of the blade at 46.6% blade span location. As was observed earlier, the intensity of sound generated decreases as we move along the blade from tip to its root.

6.3.3 At Wind speed of 13m/s

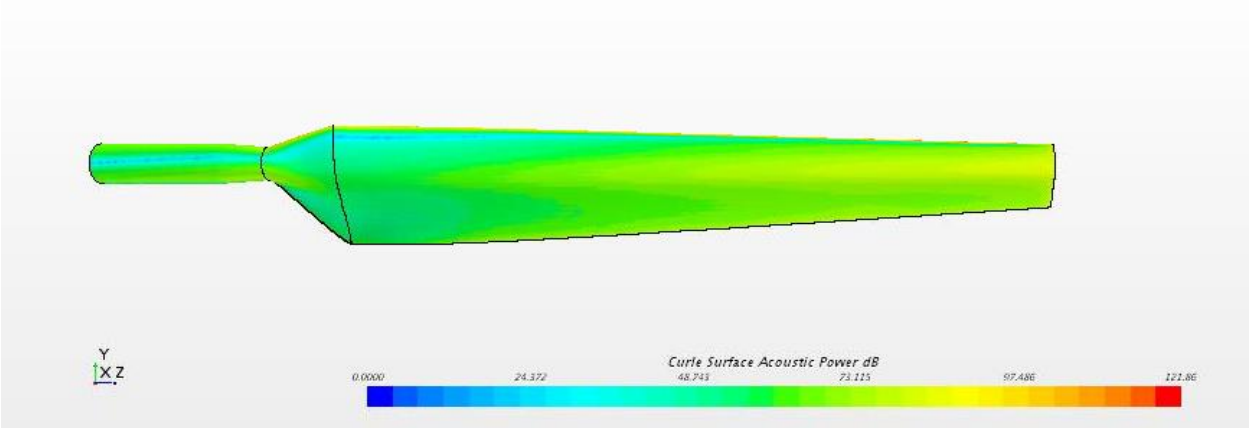

Figure 54: Sound Power Level distribution of noise sources on pressure side of blade at 13m/s.

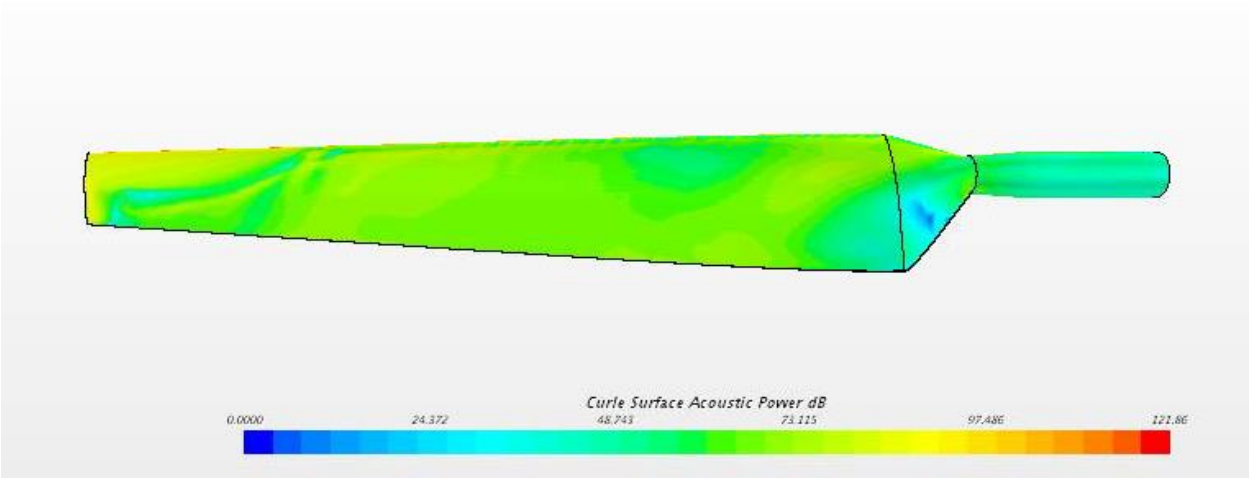

Figure 55: Sound Power Level distribution of noise sources on suction surface of blade at 13m/s.

For wind speed of 13m/s, it is clearly evident that there is an increase in noise generated by the blades when compared to 7m/s or 10m/s wind speed. The average Sound Power Level generated by majority of the blade is about 65dB with a small portion of the blade on the pressure side that generates about 35dB noise near its root. Once again, the major noise sources can be found near the blade tip.

6.3.4 <u>At Wind speed of 15m/s</u>

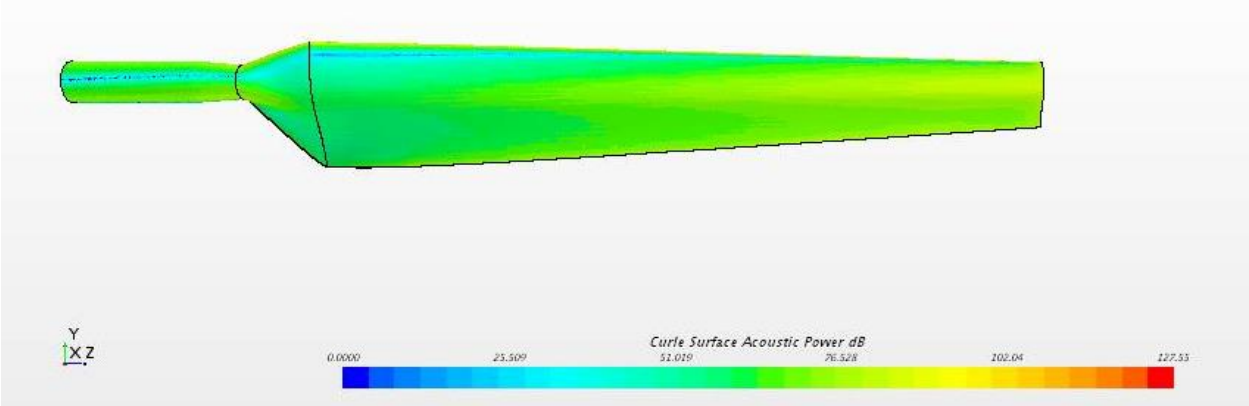

Figure 56: Sound Power Level distribution of noise sources on pressure surface of blade at 15m/s.

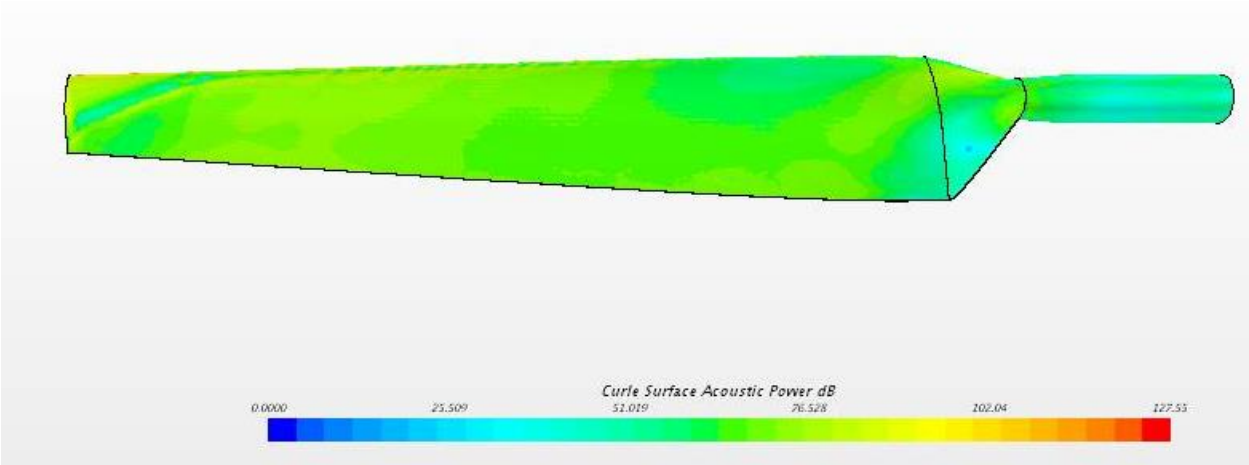

Figure 57: Sound Power Level distribution of noise sources on suction surface of blade at 15m/s.

We see that the noise generated for 15m/s is similar to that of 13m/s except that there is an increase in the amount of noise generated. The average noise generated by the blade has a Sound Power level around 70dB. The noise generated near the blade tip is the greatest and this trend decreases along the blade span.

In general, we see that there is an increasing trend in Sound Power Level generated by the blades with increase in wind speeds. We also see that the major noise sources are located near the blade tip and their intensity decreases as we move from tip to blade root along its span.

7 Conclusions

The main aim of this study was to accurately predict the aerodynamic noise generated by the NREL Phase VI rotor. This was achieved by performing aero-acoustic simulation using the accurate prediction of steady state CFD results. The steady state CFD results were validated by comparing aerodynamic and performance characteristics such as torque produced and trends of pressure coefficients at different span locations of the blade of the given rotor. Validations were performed using experimental results and previous computational work on the NREL Phase VI rotor under the same operating conditions. These simulations have been performed for four different wind speeds namely 7m/s, 10m/s, 13m/s and 15m/s. The results obtained through CFD analysis show good agreement with both experimental results and previous computational results.

The trends of pressure coefficients at different span locations are most accurate for a wind speed of 7m/s. This accuracy decreases with increase in wind speeds, a trend which is expected while using the SST k-ω turbulence model. This is because the accuracy of this model decreases with increase in flow separation that is observed at higher wind speeds.

Using the accurate predictions of flow field through steady state CFD analysis, the aerodynamic noise generated by the wind turbine blade has been predicted. This prediction includes the magnitude of noise generated in terms of Sound Power Levels and location of the noise source on the blade surface. Curle broadband noise source model is used for this prediction.

It is observed that the major noise sources are located near the tip of the blade and the intensity of noise generated decreases along the blade span towards the tip. This trend is observed for all four wind speed conditions. Furthermore, it is also observed that with increase in wind speed, there is an increase in Sound Power level generated by the blade surface.

8 Recommendations for Future Work

Now that the aerodynamic noise generated by a wind turbine rotor has been accurately predicted, these results will be considered as our basis for comparison while implementing our aerodynamic noise reduction technique.

It has been proposed that the generated aerodynamic noise can be mitigated with the usage of aero-acoustic elastomeric dampers. Though there is a sufficient literature review to support the use of elastomeric dampers to mitigate vibro-acoustic noise, elastomeric dampers used to mitigate aero-acoustic noise is an option that is less explored.

Literature review indicates a composite hydrogel that consists of number of negatively charged unilamellar titanate nano sheets that is embedded within it. Due to electrostatic repulsive forces present between these nano sheets, the hydrogel is capable of displaying anisotropic mechanical properties. These hydrogels, can easily undergo deformation when shear forces are applied parallel to the alignment of the nano sheets. However, they display high resistance to compressive forces that are applied perpendicular to the alignment of these nano sheets [39]. Based on these desirable mechanical properties, this elastomer has been chosen for our computational study. By using this elastomer as a wrap around the NREL Phase VI rotor blade, aero-acoustic simulation shall be performed to study if the aerodynamic noise has been mitigated without having significant detrimental effects on torque produced and thus power generated by the rotor.

Since the modeling of the elastomer's behavior when it interacts with the impinging wind involves complex interactions between the flexible elastomer covering the blade and impinging wind, the fluid structure interaction technique is necessary to perform this computational study. This is because both the fluid domain and the structural domain will have significant influence

on the other and thus this case cannot be solved as an exclusively fluid or an exclusively structural problem [40].

Steps involved in Fluid Structure Interaction

a. Simulations through CFD will provide pressure distributions acting on the elastomer surface. From this information, the wall forces acting on its surface can be determined.

b. These forces are inputs to structural analysis through which elastomer's deformation can be obtained as a result.

c. This deformation is taken as an input into CFD analysis, which helps in updating the existing mesh that was created.

This process is repeated several times until a stable solution is obtained for this case.

For our analysis, STAR CCM+ shall be used to as the CFD solver and PATRAN shall be used as the structural analysis solver.

9. References

1. Richardson, Jake. "America's First Wind Turbine Generated Electricity In 1888." CleanTechnica. 2014. Accessed April 02, 2016. http://cleantechnica.com/2014/06/22/americas-first-wind-turbine-generated-electricity-1888/.
2. "Third Planet Windpower." Third Planet Windpower. Accessed April 02, 2016. http://www.thirdplanetwind.com/energy/history.aspx.
3. R. Gerald Nix, " Wind Energy as a Significant Source of Electricity" NREL Report number: NREL/TP-441-8162
4. Elliot, D.L; Wendell, L.L.; Gower, G.L. "U.S. Aerial Wind Resource Estimates Considering Environmental and Land-use Exclusions." Presented at Windpower '90 Conference, Washington, D.C., September 1990.
5. S. Butterfield, S. Sheng and F. Oyague, "Wind Energy's New Role in Supplying the World's Energy: What Role will Structural Health Monitoring Play?" NREL Report number: NREL/CP-500-46180
6. "Record Chinese Installations Drive Global Market past 63 GW." GWEC. Accessed April 02, 2016. http://www.gwec.net/global-figures/wind-energy-global-status/.
7. Hau, E., and E. Hau. *Wind Turbines: Fundamentals, Technologies, Application, Economics*. Berlin: Springer, 2006.
8. Spera, David A. *Wind Turbine Technology: Fundamental Concepts of Wind Turbine Engineering*. New York: ASME Press, 1994.
9. Shepherd, Daniel, David Welch, Erinm Hill, David Mcbride, and Kimn Dirks. "Evaluating the Impact of Wind Turbine Noise on Health-related Quality of Life." *Noise Health Noise and Health* 13, no. 54 (2011): 333.
10. Klug, H., "Noise from Wind Turbines: Standards and Noise Reduction Procedures." Paper presented on the Forum Acusticum, Sevilla, Spain, 16-20 September 2002.
11. Jianu, Ofelia, Marc A. Rosen, and Greg Naterer. "Noise Pollution Prevention in Wind Turbines: Status and Recent Advances." *Sustainability* 4, no. 12 (2012): 1104-117.

12. Sagol, Ece, Marcelo Reggio, and Adrian Ilinca. "Assessment of Two-Equation Turbulence Models and Validation of the Performance Characteristics of an Experimental Wind Turbine by CFD." *ISRN Mechanical Engineering* 2012 (2012): 1-10. doi:10.5402/2012/428671.
13. Mo, Jang-Oh, and Young-Ho Lee. "CFD Investigation on the Aerodynamic Characteristics of a Small-sized Wind Turbine of NREL PHASE VI Operating with a Stall-regulated Method." *Journal of Mechanical Science and Technology J Mech Sci Technol* 26, no. 1 (2012): 81-92. doi:10.1007/s12206-011-1014-7.
14. Sorensen, N., J. Michelsen, and S. Schreck. "Navier-Stokes Predictions of the NREL Phase VI Rotor in the NASA Ames 80-by-120 Wind Tunnel." *2002 ASME Wind Energy Symposium*, 2002. doi:10.2514/6.2002-31.
15. Song, Y., and J. Perot. "CFD Simulation of the NREL Phase VI Rotor." *Wind Engineering* 39, no. 3 (2015): 299-310. doi:10.1260/0309-524x.39.3.299.
16. R P J O M Van Rooij, and E. A. Arens. "Analysis of the Experimental and Computational Flow Characteristics with Respect to the Augmented Lift Phenomenon Caused by Blade Rotation." *J. Phys.: Conf. Ser. Journal of Physics: Conference Series* 75 (2007): 012021. doi:10.1088/1742-6596/75/1/012021.
17. Ghasemian, Masoud, and Amir Nejat. "Aerodynamic Noise Prediction of a Horizontal Axis Wind Turbine Using Improved Delayed Detached Eddy Simulation and Acoustic Analogy." *Energy Conversion and Management* 99 (2015): 210-20. doi:10.1016/j.enconman.2015.04.011.
18. Tadamasa, A., and M. Zangeneh. "Numerical Prediction of Wind Turbine Noise." *Renewable Energy* 36, no. 7 (2011): 1902-912. doi:10.1016/j.renene.2010.11.036.
19. Lee, Seunghoon, and Soogab Lee. "Numerical and Experimental Study of Aerodynamic Noise by a Small Wind Turbine." *Renewable Energy* 65 (2014): 108-12. doi:10.1016/j.renene.2013.07.036.
20. Ramachandran, Rakesh C., Ganesh Raman, and Robert P. Dougherty. "Wind Turbine Noise Measurement Using a Compact Microphone Array with Advanced Deconvolution Algorithms." *Journal of Sound and Vibration* 333, no. 14 (2014): 3058-080. doi:10.1016/j.jsv.2014.02.034.

21. Hand, M. M., D. A. Simms, L. J. Fingersh, D. W. Jager, J. R. Cotrell, S. Schreck, and S. M. Larwood. "Unsteady Aerodynamics Experiment Phase VI: Wind Tunnel Test Configurations and Available Data Campaigns." 2001. doi:10.2172/15000240.
22. "S809 Airfoil Shape." S809 Airfoil Shape. Accessed May 04, 2016. http://wind.nrel.gov/airfoils/shapes/S809_Shape.html.
23. Simms, D., S. Schreck, M. Hand, and L.j. Fingersh. "NREL Unsteady Aerodynamics Experiment in the NASA-Ames Wind Tunnel: A Comparison of Predictions to Measurements." 2001. doi:10.2172/783409.
24. Raina, Amool. A., "Performance Evaluation of Wind Turbine blades using Blade Element Momentum Theory and flow simulation techniques", M.S Dissertation, Department of Aerospace Engineering, University of Kansas, 2011
25. Carcangiu, C.E., " CFD-RANS Study of Horizontal Axis Wind Turbines", Ph.D Dissertation, Dipartimento di Ingegneria Meccanica, Universita Delgi Studi Di Cagliari, Jan., 2008
26. Chen, Bindi. "Research Notes for Developers and Researchers." *Pitch-regulated and Stall-regulated Wind Turbine*. Web. 04 Apr. 2016.
27. "Siemens Student Award." *Siemens Student Award*. Web. 04 Apr. 2016.
28. International Energy Agency," Technology Roadmap-Wind energy", 2013 edition Web: https://www.iea.org/publications/freepublications/publication/Wind_2013_Roadmap.pdf
29. *Wikipedia*. Wikimedia Foundation. Web. 05 Apr. 2016.
30. F. R. Menter, " Two-Equation Eddy viscosity Turbulence Models for Engineering Applications. AIAA Journal 32(8): 1598-1605, August 1994.
31. "ANSYS Fluent 12.0 User's Guide." https://uiuc-cse.github.io/me498cm-fa15/lessons/fluent/refs/ANSYS Fluent Theory Guide.pdf.
32. Wagner, S., R. Bareiss, and G. Guidati. *Wind Turbine Noise*. Berlin: Springer, 1996.
33. "What Is Noise?" BRD Noise & Vibration Control, Inc. Accessed April 19, 2016. http://www.brd-nonoise.com/RequestDetails.aspx.
34. "Acoustics and Vibration Animations." Sound Fields Radiated by Simple Acoustic Sources. Accessed April 19, 2016. http://www.acs.psu.edu/drussell/Demos/rad2/mdq.html.

35. "What Is Aeroacoustics?" STAR CCM User Guide, http://stevedocs.cd-adapco.com/ViewDocs/authdocs/starccmplus_latest_en/index.html#page/STARCCMP/GUID-F0F38A93-0771-4AA1-90DA-D0068D9F2BB5=en=.html.
36. Brentner, Kenneth S., and F. Farassat. "Analytical Comparison of the Acoustic Analogy and Kirchhoff Formulation for Moving Surfaces." *AIAA Journal* 36 (1998): 1379-386. doi:10.2514/3.13979.
37. "Dipole and Quadrupole Broadband Noise Sources" STAR CCM User Guide http://stevedocs.cd-adapco.com/ViewDocs/authdocs/starccmplus_latest_en/index.html#page/STARCCMP/GUID-4975D519-492A-4774-998B-98AD6C592796=en=.html#wwID0E3GYMB.
38. "Curle" STAR CCM User Guide http://stevedocs.cd-adapco.com/ViewDocs/authdocs/starccmplus_latest_en/index.html#page/STARCCMP/GUID-A92915B9-EF9C-4FD3-BF99-19C77F3E6F16=en=.html#wwID0EW22MB.
39. Liu, Mingjie, Yasuhiro Ishida, Yasuo Ebina, Takayoshi Sasaki, Takaaki Hikima, Masaki Takata, and Takuzo Aida. "An Anisotropic Hydrogel with Electrostatic Repulsion between Cofacially Aligned Nanosheets." *Nature* 517, no. 7532 (2014): 68-72. doi:10.1038/nature14060
40. Krawczyk, Piotr, Asfaw Beyene, and David Macphee. "Fluid Structure Interaction of a Morphed Wind Turbine Blade." *International Journal of Energy Research Int. J. Energy Res.* 37, no. 14 (2013): 1784-793. doi:10.1002/er.2991.